Preliminary results of the impact of lightning and radar reflectivity factor data assimilation on the very short term rainfall forecasts of RAMS@ISAC: application to two case studies in Italy

Stefano Federico[1], Rosa Claudia Torcasio[1], Elenio Avolio[2], Olivier Caumont[3], Mario Montopoli[1], Luca Baldini[1], Gianfranco Vulpiani[4], Stefano Dietrich[1]

1. ISAC-CNR, via del Fosso del Cavaliere 100, Rome, Italy
2. ISAC-CNR, zona Industriale comparto 15, 88046 Lamezia Terme, Italy
3. CNRM UMR 3589, University of Toulouse, Météo-France, CNRS, 42 avenue G. Coriolis, 31057 Toulouse, France
4. Dipartimento Protezione Civile Nazionale Ufficio III - Attività Tecnico Scientifiche per la Previsione e Prevenzione dei Rischi, 00189 Rome

Abstract

In this paper, we study the impact of lightning and radar reflectivity factor data assimilation on the precipitation VSF (Very Short-term Forecast, 3 hours in this study) for two relevant case studies occurred in Italy. The first case refers to a moderate and localised rainfall over central Italy occurred on 16 September 2017. The second case, occurred on 9 and 10 September 2017, was very intense and caused damages in several geographical areas, especially in Livorno (Tuscany) where nine people died.

The first case study was missed by several operational forecasts (from both public and private sectors), including that performed by the model used in this paper, while the Livorno case was partially predicted by operational models.

We use the RAMS@ISAC model (Regional Atmospheric Modelling System at Institute for Atmospheric Sciences and Climate of the Italian National Research Council), whose 3D-Var extension to the assimilation of RADAR reflectivity factor is shown in this paper for the first time.

Results for the two cases show that the assimilation of lightning and radar reflectivity factor, especially when used together, have a significant and positive impact on the precipitation forecast. For specific time intervals, the data assimilation is of practical importance for civil protection purposes because changes a missed forecast of intense precipitation ($\geq$ 40 mm/3h) in a correct one.

While there is an improvement of the rainfall VSF thanks to the lightning and radar reflectivity factor data assimilation, its usefulness is partially reduced by the increase of the false alarms, especially when both data area assimilated.

Keywords: data assimilation, lightning, radar reflectivity factor, RAMS@ISAC.

1. Introduction

Initial conditions of numerical weather prediction (NWP) models are a key point for a good forecast (Stensrud and Fritsch, 1994; Alexander et al., 1999). Nowadays limited area models are operational at the resolution of few kilometres (< 5 km) and data assimilation of non-conventional observations, as lightning or radar data, is crucial to correctly represent the state of the atmosphere at local scale (Weisman et al., 1997; Weygandt et al., 2008). This is especially important over the sea, where the absence of local observations and model deficiencies can misrepresent convection.

The assimilation of radar reflectivity factor[1] is useful to improve the weather forecast considering the high repetition rate (asynoptic data) and the high spatial resolution (local scale) of the radar data.

First attempts to assimilate radar reflectivity factor are reported in Sun and Crook (1997, 1998), who expanded VDRAS (Variational Doppler Radar Analysis System) to include microphysical retrieval. Following these studies, several systems to assimilate radar observations, both Doppler velocity and reflectivity factor, were developed (Xue et al., 2003, Zhao et al., 2006; Xu et al., 2010). All these studies showed the stability and robustness of assimilating radar observations as well as the improvement of weather forecast.

Radar data are also assimilated in WRF (Weather Research and Forecasting model, Skamarock et al., 2008; Barker et al., 2012) both using 3DVar (Xiao et al., 2005, 2007; Barker et al., 2004) and 4DVar (Wang et al., 2013; Sun and Wang, 2012). The capability to assimilate radar data into WRF was recently applied to a heavy rainfall event over Central Italy by Maiello et al. (2014). They showed a notable and positive impact of the radar data assimilation on the precipitation forecast, also when radar data were assimilated together with conventional data (SYNOP and RAOB).

In addition to direct methods, which assimilate the radar reflectivity factor adjusting the hydrometeor contents, there are indirect methods adjusting other variables. In particular, the method of Caumont et al. (2010) acts on the relative humidity field. It consists of two different steps: a 1D retrieval of relative humidity (pseudo-profile), which depends on the radar reflectivity factor observations, followed by 3D-Var assimilation of the pseudo-profile. This method has the advantage to reduce the computational cost at the kilometric scale.

---

[1] Throughout the paper we use the expression radar reflectivity factor, which is the quantity provided by the radar (and expressed in mm^6m^{-3} or dBz) after conversion from the received power. The radar reflectivity factor is different from reflectivity and is obtained in the special case of Rayleigh scattering. Reflectivity is not the quantity that radars usually provide and display on their screens although most of people refer to it.

67 The choice of updating the moisture field directly is motivated by its greater impact on analyses
68 and forecasts in comparison to that of hydrometeor-related quantities (e.g., Fabry and Sun, 2010).
69 Caumont et al. (2010) showed that the method improved the weather prediction of a heavy
70 precipitation event in southern France and of a eight-day long assimilation cycle experiment.
71 The method was applied in other studies (Wattrelot et al., 2014, using AEROME model; Ridal and
72 Dalbom, 2017; using HARMONIE model), or modified using 4D-Var in place of 3D-Var (Ikuta and
73 Honda, 2011; using JNoVa model) showing its capability to improve the weather forecast. The
74 method is also used in the operational context (Wattrelot et al., 2014).
75 Flashes are another important source of asynoptic data due to their ability to locate precisely the
76 convection with few temporal gaps (Mansell et al., 2007). In the last two decades, there have been
77 attempts to assimilate lightning into meteorological models both at low horizontal resolution,
78 which need a cumulus parameterization scheme to simulate convection, and at convection
79 permitting scales.
80 The first attempts to assimilate lightning in NWP models were based on relationships between
81 lightning and rainfall rate estimated by microwave sensors on board polar satellites (Alexander et
82 al., 1999; Chang et al., 2001; Jones and Macpherson, 1997; Pessi and Businger, 2009). In this
83 approach, the rainfall rate was computed as a function of lightning observations and then
84 transformed into latent heat, which was assimilated. The results of these studies showed a
85 positive impact of the lightning data assimilation on the forecast up to 24h also for fields at the
86 large scale, as sea-level pressure.
87 The study of Papadopulos et al. (2005) used lightning to locate convection and the model water
88 vapour profile was nudged towards vertical profiles recorded during convective events.
89 Mansell et al. (2007) modified the Kain-Fritsch (Kain and Fritsch, 1993) cumulus convective scheme
90 to force convection when/where flashes are observed while the convective scheme was not
91 activated in the model simulation, demonstrating the potential of lightning to improve the
92 convection forecast. A similar approach was introduced by Giannaros et al. (2016) into WRF
93 showing the positive impact of lightning data assimilation on the precipitation forecast up to 24h
94 for eight convective events occurred over Greece.
95 Fierro et al. (2012) introduced a methodology to assimilate lightning at convection permitting
96 scales by modifying the water vapour mixing ratio simulated by the WRF according to a function
97 depending on the flash-rate and on the simulated graupel mixing ratio. The water vapour could be
98 assimilated by nudging (Fierro et al., 2012) or 3D-Var (Fierro e al., 2016).

99 Qie et al. (2014), using WRF, extended the methodology of Fierro et al. (2012) to assimilate ice

100 crystals, graupel and snow, showing promising results for deep convective events in China.

101 Fierro et al. (2015) studied the performance of the Fierro et al. (2012) method for 67 days

102 spanning the 2013 warm season over the CONUS giving a statistically robust estimation of the

103 performance of the method. The computationally inexpensive lightning data assimilation method

104 improved considerably the short-term (≤ 6h) precipitation forecast of high impact weather.

105 Lynn et al. (2015), Lynn (2017) also applied the method of Fierro et al. (2012) to boost the local

106 thermal buoyancy where/when lightning is observed. Results show that lightning data assimilation

107 improved lightning forecast. Importantly, Lynn et al. (2015) offer an approach to address spurious

108 convection (i.e., convection removal), which is a far more challenging problem to tackle.

109 Federico et al. (2017a) implemented the methodology of Fierro et al. (2012) in RAMS@ISAC

110 model, showing the systematic and significant improvement of the precipitation forecast at the

111 very short range (3h) for twenty case studies occurred over Italy; the impact of lightning data

112 assimilation for longer time ranges (6h-24h; Federico et al., 2017b) showed considerable impact

113 on the 6h precipitation forecast, with smaller (negligible) effects at 12 h (24 h).

114 In this paper, we study the impact of radar reflectivity factor and lightning data assimilation on the

115 very short term (3h) rainfall prediction for two case studies over Italy. We use the method of

116 Fierro et al. (2012) to assimilate lightning and the method of Caumont et al. (2010) to assimilate

117 the radar reflectivity factor. The case studies occurred in September 2017. The first case, hereafter

118 also referred to as Serano, occurred on 16 September, was characterized by moderate-intense and

119 localized rainfall. The second case, hereafter also referred to as Livorno, occurred on 09-10

120 September, was characterized by deep convection and very intense precipitation in several parts

121 of Italy. Even if the Livorno case occurred before the Serano case, we reverse the chronological

122 order in the discussion, ordering the event from the less intense to the most intense.

123 The forecast of severe events at the local scale still remains a challenge because of the multitude

124 of physical processes involved over a wide range of scales (Stensrud et al., 2009). The Serano case

125 study, being localized in space, poses challenges in forecasting the exact position and timing of

126 convection initiation; the Livorno event involves the interaction between a high impact storm and

127 the complex orography of Italy, which is difficult to simulate at the local scale. For the above

128 reasons the forecast of both events was challenging, as confirmed by the poor forecast of

129 RAMS@ISAC. The difficulty to forecast timely and accurately the precipitation field is the reason

130 for choosing them as test cases.

This paper presents for the first time the assimilation of the total lightning (intra cloud + cloud to ground) and radar reflectivity factor in RAMS@ISAC and shows how the assimilation of the radar reflectivity factor works together with total lighting data assimilation. Also, this paper shows how accurate in space and time can be the forecast of the precipitation field using cloud scale observations over complex terrain, contributing in this way to a number of works on the same subject.

The paper is organized as follows: Section 2 gives details on the synoptic environment of the case studies showing daily precipitation, lightning and radar observations; Section 3 gives details on the meteorological model, lightning and radar data assimilation; Section 4 shows the results for three very short-term forecast (VSF), one for Serano and two for Livorno; Discussion and conclusions are given in Section 5. This paper has additional material where we discuss: a) how the lightning and radar reflectivity factors data assimilation adjust the total water field; b) the sensitivity of the results to the choice of key parameters of lightning data assimilation.

2. The case studies

2.1 The 16 September 2017 (Serano) case study

During the 16 September 2017 Italy was under the influence of a cyclone that developed to the lee of the Alps. The storm crossed Italy from NW to SE leaving light precipitation over most of the peninsula with moderate rainfall over Central Italy. Figure 1 shows the precipitation recorded by the Italian raingauge network on 16 September 2017. Light precipitation (< 5 mm/day) is reported by 1018 raingauges out of the 1666 stations measuring precipitation ($\geq$ 0.2 mm/day) on this day. Fourteen stations over Central Italy recorded more than 50 mm/day. The maximum precipitation was 90 mm/day in Città di Castello (Umbria Region, Figure 1). Because the meteorological radar closest to the maximum precipitation is over mount Serano (Figure 1), hereafter this event will be referred to as Serano.

The synoptic condition during the event is shown in Figure 2. At 500 hPa (Figure 2a) a trough, elongated in the SW-NE direction, extends over Western Europe and air masses are advected from SW towards western Alps. The interaction between the airflow and the Alps generates a low pressure to the lee of the Alps over Northern Italy.

The analysis at the surface (Figure 2b) shows the meteorological front represented by the equivalent potential temperature gradient between air masses advected over the Mediterranean

Sea from NW and air masses advected from the South over the Tyrrhenian Sea. Notable is the feeding of warm unstable air masses towards Central Italy.

Infrared satellite images (Figure 3), from 00 UTC on 16 September to 00 UTC on 17 September, show the cold front structure moving slowly from NW to SE. Interestingly, at 00 UTC on 16 September, it is apparent the well-defined cloud system over Central Italy (red circle of Figure 3a), which caused most of the daily precipitation observed between 43.50 and 45.0 N in the six-hours 00 UTC-06 UTC on 16 September.

The well-defined cloud system over Central Italy is also evident in the radar Constant Altitude Plan Position Indicator (CAPPI) at 3 km above sea level at 02 UTC on 16 September (Figure 4). This CAPPI is formed by interpolating all the available data from the federated Italian radar network coordinated by the Department of Civil Protection (twenty-two radars, see Section 3.3 for their positions) and it is also referred to as the national radar composite (hereafter also mosaic). Several convective cells exceeding 35 dBz can be noted over central-northern Italy. Importantly, the cloud system over Central Italy shown by the satellite infrared channel at 00 UTC (Figure 3a) and that of the radar at 02 UTC have similar positions, showing that the cloud system was active for several hours over Central Italy.

Figure 5 shows the lightning recorded by the LINET network (Betz et al., 2009) on 16 September 2017. More than 105.000 flashes were recorded during the day; most of them occurred during the afternoon and evening, but a secondary maximum occurred in the night, from 00 UTC to 06 UTC. In this phase, more than 3000 flashes were observed over Central Italy.

2.2 The 09-10 September 2017 (Livorno) case study

During the days 09 and 10 September 2017, Italy was hit by a severe storm characterised by intense and widespread rainfall over the country. Figure 6a shows the precipitation on 09 September recorded by the Italian raingauge network. Rainfall was intense over the Alps, where the maximum daily precipitation was observed (193 mm/day) and over Liguria, with precipitation of the order of 30-50 mm/day. One station over Tuscany reported 90 mm/day, showing that intense precipitation already started over the Region. The intensity of the storm on 09 September was high because 20 raingauges reported more than 100 mm/day and 70 raingauges more than 60 mm/day, and, in most cases, this precipitation occurred within few hours.

The following day (see Figure 6b) had higher rainfall. Precipitation occurred mainly over Central Italy, especially over Lazio, and over Northern Italy, in particular the North-East. In Tuscany, the

194 two stations close to the sea, in the Livorno area, recorded about 150 mm/day mostly fallen in the

195 hours between 00 and 06 UTC. The rainfall on 10 September was abundant: and 60 raingauges

196 recorded more than 100 mm/day.

197 Synoptic conditions leading to this storm are shown in Figure 7. At 500 hPa (Figure 7a) a trough

198 extends from Northern Europe towards the Mediterranean. The interaction between the air-

199 masses and Western Alps generated a depression to the lee of the Alps, which crossed the whole

200 peninsula from NW to SE. It is noted the divergent flow over Central and Northern Italy favouring

201 upward motions.

202 At the surface, Figure 7b, it is evident the equivalent temperature gradient over the western

203 Mediterranean caused by the contrast between air masses pre-existing over the sea and air

204 masses advected from France towards the Mediterranean. The pressure field at the surface

205 advects air masses from the South over the Tyrrhenian Sea. These warm and humid air masses

206 feed the cyclone during its development.

207 From a synoptic point of view, Livorno and Serano cases are similar and represent two cyclones

208 developing to the lee of the Alps (Buzzi and Tibaldi, 1978). However, the Livorno case is more

209 intense than Serano as shown by the larger rainfall occurred in the former case.

210 The notable intensity of the Livorno case is confirmed by the lightning observations (Figure 8).

211 During the evening of 9 September (after 18 UTC) about 38.000 flashes were recorded by LINET.

212 On 10 September about 290.000 flashes were recorded over Italy, following the movement of the

213 storm propagating from NW to SE. So, more than 300.000 flashes were recorded from 18 UTC on

214 09 September to 00 UTC on 11 September, which are more than three times those recorded for

215 Serano.

216 Thermal infrared satellite images (channel, 10.8 micron; Figure 9) show the extension of the cloud

217 coverage every 12 hours. It is well evident the cloud system associated with the cold front over

218 Europe. More specifically, the satellite image at 00 UTC shows the cloud system over Livorno area

219 (red circle in Figure 9b), before the main precipitation event over Tuscany (00-06 UTC), while

220 Figure 9c shows the cloud system over Central Italy (orange circle), at the end of the period of

221 intense precipitation over Lazio (06-12 UTC).

222 We conclude the synoptic analysis of the case study with two CAPPI at 3 km observed by the radar

223 network of the Department of Civil Protection. The CAPPI in Figure 10a, at 00 UTC on 10

224 September, shows the cloud system over Tuscany with reflectivity factor up to 40 dBz. Other

225 clouds cause rainfall over northern Italy. The CAPPI of Figure 10a is the last assimilated by the 00-

226 03 UTC VSF on 10 September shown in Section 4.2.1.

227 Figure 10b shows the CAPPI of the national radar mosaic at 3 km above the sea level and at 06

228 UTC. The cloud system is moving towards Central Italy with reflectivity up to 45 dBz. Other cloud

229 systems are apparent over northern Italy. Figures 10a-10b well represent the movement of the

230 storm towards SE and Figure 10b shows the last CAPPI assimilated by the 06-09 UTC VSF shown in

231 Section 4.2.2.

232

233 **3.Data and Methods**

234 *3.1 RAMS@ISAC and simulations set-up*

235 The RAMS@ISAC is used as NWP driver in this work. The model is based on the RAMS 6.0 model

236 (Cotton et al., 2003) with the addition of four main features, as well as a number of minor

237 improvements. First, it implements additional single moment microphysical schemes, whose

238 performance is shown in Federico (2016): among them, the WSM6 (Hong and Lim, 2006) is used in

239 this paper. Second, it predicts the occurrence of lightning following the diagnostic method of Dahl

240 et al. (2011), the implementation being discussed in Federico et al. (2014). Third, the model

241 assimilates lightning through nudging (Fierro et al., 2012, 2015; Federico et al., 2017a). Fourth, the

242 model implements a 3D-Var data assimilation system (Federico, 2013, hereafter also RAMS-

243 3DVar), whose extension to the radar reflectivity factor is presented in this paper (Section 3.3).

244 The list of the main physical parameterisation schemes used in the simulations of RAMS@ISAC is

245 shown in Table 1.

246 Considering the domains and the configuration of the grids (Figure 11 and Table 2), two different

247 set-ups are used for Serano and Livorno. For the first case, we use the domains D1 and D2, while

248 for Livorno we use also the domain D3. The first domain covers a large part of Europe and extends

249 over the North Africa. For this domain, the horizontal resolution of the grid is 10 km (R10). The

250 second domain extends over the whole Italy and part of Europe and the grid has 4 km horizontal

251 resolution (R4). The third domain covers the Tuscany Region, has 4/3 km horizontal resolution

252 (R1), and it is used for Livorno to represent with higher spatial detail the precipitation field over

253 Tuscany. The fine structures of the precipitation field are smeared out over Tuscany using only

254 domains D1 and D2. The operational implementation of the RAMS@ISAC model uses the domains

255 D1 and D2 and no refinements for specific areas of Italy are used because Italy is a complex

orography country and grid refinements for a specific event can be done only a-posteriori, i.e. after the occurrence of the event.

The resolution and the extension of the grids in the vertical direction is the same for the three domains. The vertical grid covers the troposphere and the lower stratosphere. Vertical levels have different spacings and are more packed close to the ground. Among the 36 levels used in this paper 10 are below 1 km, 15 below 2 km and 18 below 3 km. The first vertical level is at 24 m above the surface in the terrain following coordinates used by RAMS@ISAC, the level 21 is at 5200 m. Above 6 km the model levels are about 1000 m apart, with a maximum of 1200 m for the vertical layer at the model top.

The vertical grid is the same as the operational setting of RAMS@ISAC and is a compromise between vertical resolution and computing time. In the future, the number of vertical levels will be increased to better resolve the phenomena in this direction (Planetary Boundary Layer processes, vertical motions, interaction between air masses and orography etc.), nevertheless the current setting was used successfully in the forecast of several heavy precipitation events over Italy. The nesting between the first and second domains is one-way, while the nesting between the second and the third domains is two-way.

VSF is implemented as shown in Figure 12. First a run with R10 configuration is performed using the 0.25° horizontal resolution GFS analysis/forecast cycle issued at 12 UTC as initial and boundary conditions. R10 run, which starts at 12 UTC on 16 September for Serano and at 12 UTC on 09 September for Livorno, lasts 36 h and doesn't assimilate neither radar reflectivity factor nor lightning. The R10 run is not updated after the acquisition of new data by the analysis system and this is a limitation of the results shown in this paper.

Starting from 12 UTC, ten VSF are performed using R4 for Serano and both R4 and R1 for Livorno. The VSF lasts 9h and uses R10 simulation as initial and boundary conditions (one-way nesting). The 9h forecast is divided into two parts: the first six hours are the assimilation stage when RAMS@ISAC simulation is adjusted by data assimilation, whereas the last three hours are the forecast stage, without data assimilation. During the assimilation stage, flashes are assimilated by nudging (Section 3.2), while radar reflectivity factor is assimilated every one-hour by RAMS-3DVar (Caumont et al. (2010), Section 3.3).

It is noted that data assimilation is performed over the domain D2 (R4) only, and the innovations are transferred to the domain D3 (R1), for the Livorno case, by the two way-nesting. The domain D3 is used for the Livorno case to refine the resolution of the precipitation field over Tuscany and

to show the spatial and temporal precision of the precipitation forecast over Tuscany using data assimilation. However, its usage is exceptional because, as stated above, Italy is a complex orography country and grid refinements for specific areas are used only after the occurrence of the event. For this reason, the domain D3 is usually not used in RAMS@ISAC and no statistics about the background error are available for this grid.

Because lightning and radar reflectivity factor are cloud scale observations, their assimilation at higher horizontal resolution by 3D-Var is foreseeable in future works.

The verification of the VSF for precipitation is done by visual comparison of the model output with the raingauge network of the Department of Civil Protection, which has more than 3000 raingauges all over Italy.

In addition we consider the FBIAS (Frequency Bias; range [0, + ∞)), where 1 is the perfect score, i.e. when no misses and false alarms occur), POD (Probability of Detection; range [0, 1], where 1 is the perfect score and 0 the worst value) and ETS (Equitable Threat Score; range [-1/3,1], where 1 is the perfect score and 0 is a useless forecast). Scores are computed from 2x2 dichotomous contingency tables (Wilks, 2006) for different rainfall thresholds.

3.2 Lightning data assimilation

Lightning data are provided by LINET (LIghtning detection NETwork; Betz et al., 2009; www.nowcast.de) which has more than 500 sensors worldwide with the greatest density over Europe (more than 200 sensors). The network has a good coverage over Central Europe and Western Mediterranean (from 10 W to 35 E and from 30 N to 60 N). The area of good coverage includes the region considered in this paper.

LINET exploits the VLF/LF electromagnetic bands and provides measurements of both intra-cloud (IC) and cloud to ground (CG) discharges. IC strokes are detected as long as lightning occurs within 120 km from the nearest sensor thanks to an optimised hardware and advanced techniques of data processing (TOA-3D, Betz et al., 2004). According to Betz et al. (2009), LINET has a location accuracy of 125 m for an average distance of 200 km among the sensors verified by strikes into towers of known positions.

The good performance of the LINET network and its ability to detect IC strokes is shown in Lagouvardos et al. (2009) for a storm in southern Germany, while the good performance over Italy, including both CG and IC strokes, is discussed in Petracca et al. (2014).

The lightning data assimilation scheme is that of Fierro et al. (2012; 2014; 2015) and uses the total lightning, i.e. intra-cloud plus cloud to ground flashes.

321   The method starts by computing the water vapour mixing ratio q_v:

322    $$q_v = Aq_s + Bq_s \tanh(CX)(1 - \tanh(Dq_g^\alpha))$$ (1)

323   Where coefficients are set to A=0.86, B=0.15, C=0.30, D=0.25, α=2.2, q_s is the saturation mixing

324   ratio at the model atmospheric temperature, and q_g is the graupel mixing ratio (g kg^{-1}). X is the

325   number of total flashes (IC+CG) falling in a grid box of domain D2 (R4) in the past five minutes. The

326   mixing ratio q_v of Eq. (1) is computed only for grid points where flashes are recorded. More

327   specifically, for each grid point we consider the number of flashes falling in a grid box centred at

328   the grid point in the last five minutes. The mixing ratio of Eqn. (1) is compared with that predicted

329   by the model. If the mixing ratio of Eqn. (1) is larger than the simulated one, the latter is nudged

330   towards the value of Eqn. (1), otherwise the modelled mixing ratio is left unchanged. This method

331   can only add water vapour to the forecast.

332   The check and eventual substitution of the water vapour is performed every five minutes and it is

333   made within the mixed phase layer zone (0 °C, -25°C), wherein electrification processes caused by

334   the collision of ice and graupel are the most active (Takahashi 1978, Emersic and Sounders, 2010;

335   Fierro et al., 2015).

336   The scheme of Fierro et al. (2012; 2015) was adapted to RAMS@ISAC in Federico et al. (2017a). In

337   particular, the coefficient C of Eqn. (1) was rescaled from that of Fierro et al. (2012) considering

338   the different spatial and temporal resolution of the gridded lightning data; then the coefficient C

339   was tuned (increased) by trials and errors considering two case studies of HyMeX-SOP1 (15 and 27

340   October 2012). The C constant was adapted subjectively considering two opposite requests:

341   increasing the hits and minimising false alarms. POD and ETS scores were considered as metrics

342   for this purpose. Then, Eqn. (1) was applied to twenty case studies of HyMeX-SOP1 giving a

343   statistically significant (90, or 95% depending on the rainfall threshold) improvement of the

344   RAMS@ISAC precipitation VSF (3h).

345   Nevertheless, an exhaustive statistic on the performance of rainfall VSF to nudging formulation in

346   RAMS@ISAC is missing and further studies are needed in this direction. Also, the optimal choice of

347   the coefficients A, B, C, D and α is case dependent.

348   Fierro et al (2012) applied the method using the ENTLN network, which has a detection efficiency

349   (DE) greater than 50% for IC over Oklahoma, where the ENTLN data were used. The emphasis on

350   IC flashes in the set-up of Fierro et al. (2012) is given because observational and model studies

351   have provided evidence that IC flashes correlate better than CG flashes with various measures of

352   intensifying convection (updraft strength, volume, graupel mass flux etc.; MacGorman et al. 1989;

353   Carey and Rutledge 1998; MacGorman et al. 2005; Wiens et al. 2005; Kuhlman et al. 2006; Fierro

354   et al. 2006; Deierling and Petersen 2008; MacGorman et al. 2011). For this reason methods that

355   use both IC and CG flashes performs better than those using CG only, being CG flashes correlated

356   with the descent of reflectivity cores and the onset of the demise of the storm' s updraft core

357   (MacGorman and Nielsen, 1991).

358   The analysis of the case studies shows that IC strokes are about 30% of the total number of strokes

359   reported. Also, the fraction of IC strokes to the total strokes depends on the position. For example,

360   for the Serano case, the fraction of IC strokes detected by LINET over the area hit by the largest

361   precipitation is more than 50% while over the Adriatic Sea it decreases to 10%.

362   It is also noted that DE for IC strokes cannot be reliably compared between LINET and ENTLN,

363   because the area is different and the technical details about IC detection remain unclear (type of

364   signals, VLF/LF or VHF, discrimination IC-CG).

365   For all the above reasons the application of the Fierro method to RAMS@ISAC is not

366   straightforward and it is appropriate to study the dependence of the rainfall VSF to the nudging

367   formulation. This subject is studied in the supplemental material of this paper (Section S.2) and

368   the results show that the choice of the coefficient of Eqn. (1) used in this paper is reasonable.

369   It is finally noted that despite the limitations noted above, the lightning data assimilation, as used

370   in this paper, has a significant and positive impact on RAMS@ISAC rainfall VSF (Federico et al.,

371   2017a; 2017b).

372

373

374   *3.3 Radar data assimilation*

375   The method assimilates CAPPI of radar reflectivity factor operationally provided by the Italian

376   Department of Civil Protection (DPC). Radar data are provided over a regular Cartesian grid with 1

377   km horizontal resolution and for three vertical levels (2, 3, 5 km above the sea level). The CAPPIs

378   at 2, 3, and 5km can be considered as under-sampled vertical profiles. CAPPIs are composed

379   starting from the 22 radars of the Italian Radar Network (Figure 13) 19 operating at the C-band

380   (i.e., 5.6 GHz) and 3 at X-band (i.e., 9.37 GHz). Data quality control and CAPPI composition is

381   performed by DPC. Data quality processing chain aims at identifying most of the uncertainty

382   sources as clutter, partial beam blocking and beam broadening. The radar observations are

383   processed according to nine steps detailed in Vulpiani et al. (2014), Petracca et al. (2018) and

384   references therein.

385 Radial velocity is not assimilated into RAMS@ISAC because it is not operationally processed, the

386 scan strategy being optimized for QPE purposes. Furthermore, the implementation of a radial

387 velocity data assimilation scheme is under development in RAMS-3DVAR and it is not currently

388 available for testing. For these reasons, we didn't consider the assimilation of this parameter.

389 Before entering data assimilation, the Cartesian grid is reduced to 5 km by 5 km by choosing one

390 point every five of the Cartesian grid provided by DPC in order to reduce the numerical cost of the

391 data assimilation and to reduce the effect of correlated observation errors (Rohn et al., 2001). The

392 radar grid (Figure 4, for example) is then a Cartesian grid with 5 km grid-spacing and three vertical

393 levels.

394 It is important to note the pure sampling of the data could result in implementation of errors (for

395 example reflectivity given by insects or birds) or extremes. Creating superobservations would

396 reduce this problem, the main drawback being the missing of very localised phenomena. While

397 the aim of this paper is to present the update of the data assimilation system of RAMS@ISAC and

398 its application to two challenging cases, the problem of using superobservations will be considered

399 in future studies because it impacts the results.

400 The methodology to assimilate radar reflectivity factor is that of Caumont et al. (2010), named

401 1D+3DVar, which is a two-step process: first, using a Bayesian approach inspired to GPROF

402 (Goddard Profiling Algorithm; Olson et al., 1996; Kummerow et al., 2001), 1D pseudo-profiles of

403 model variables are computed, then those pseudo-profiles are assimilated by 3DVar. Both steps

404 are discussed below.

405 The first step computes a pseudo-profile of relative humidity weighting the model profiles of

406 relative humidity around the radar profile (Bayesian approach). The pseudo-profile is computed

407 by:

$$\mathbf{z_o^p} = \frac{\sum_i \mathbf{RH_i} W_i}{\sum_j W_j}$$

408   (2)

409 Where RH_i is the RAMS@ISAC vertical profile of relative humidity at a grid point inside a square of

410 50*50 km^2 centred at the radar vertical profile, W_i is the weight of each profile and $\mathbf{z_o^p}$ is the

411 relative humidity pseudo-profile. The summation is taken over all the grid points inside a square of

412 50*50 km^2 around the observed profile and the denominator is a normalisation factor. The

413 weights are determined by the agreement between the simulated and observed reflectivity factor:

$$W_i = \exp\left\{ -\frac{1}{2}\left[\mathbf{z_o} - h_z(x_i)\right]^T \mathbf{R_z^{-1}}\left[\mathbf{z_o} - h_z(x_i)\right]\right\} \tag{3}$$

414

415 Where h_z is the forward observation operator, transforming the background column $\mathbf{x_i}$ into the

416 observed reflectivity factor. The forward radar observation operator is taken from the RIP

417 (Read/Interpolate/Plot) software (https://dtcenter.org/wrf-

418 nmm/users/OnLineTutorial/NMM/RIP/index.php, last access 03 March 2019) and is given in the

419 supplemental material of this paper (Section S4). It assumes a Marshall-Palmer hydrometeors size-

420 distribution, Rayleigh scattering, and depends on the mixing ratios of rain, graupel and snow.

421 The matrix $\mathbf{R_z}$ in Eqn. (3) is diagonal and its value is $n\sigma^2$, where σ is 1 dBz and n is the number of

422 available observations in the vertical profile (from 1 to 3). In this way, we give more weight to

423 vertical profiles containing more data.

424 The error of radar data is assumed small (1dBz) for two reasons: a) reflectivity data are carefully

425 checked by the Civil Protection Department; b) the performance of control simulation, not

426 assimilating any data, is rather poor for the case studies. This setting, however, could not be

427 optimal for cases when the control forecast performs better.

428 It is important to point out that the 50 km length-scale of the above step doesn't represent the

429 horizontal correlation length-scale of the background error, which determines the horizontal

430 spread of the innovations in the 3D-Var data assimilation (the latter length-scale is between 14

431 and 25 km depending on the level). The 50 km length-scale is used to set a square for computing

432 the pseudo-profile of relative humidity (Eqn. (2)). This profile is given by a weighted average

433 whose weights are determined by the agreement between the simulated and observed reflectivity

434 factor. The larger the agreement the larger the weight. This distance is appropriate because the

435 spatial error of meteorological models in simulating meteorological features, for example fronts,

436 can be of this order. The control simulation of the two events considered in this paper confirms

437 this choice.

438 The method is not able to force convection when the model has no rain, snow or graupel in a

439 square around (50*50 km^2) a radar profile with reflectivity factor greater than zero. In this case,

440 the pseudo-profile of relative humidity is assumed saturated above the lifting condensation level

441 and with no data below (Caumont et al., 2010).

442 It is also noted that the method is able to reduce spurious convection when the reflectivity factor

443 is simulated but not observed, because the pseudo-profile of relative humidity gives more weight

444 to the drier relative humidity profiles simulated by RAMS@ISAC inside the 50*50 km^2 square

centred at the radar profile. Of course, the ability to reduce spurious convection depends on the availability of dry model profiles around the specific radar profile (see the example below). Finally, if the observed profile is dry and the profile simulated by RAMS@ISAC is dry too, the pseudo-profile is not computed.

In summary, pseudo-profiles are computed for each profile of the radar grid whenever reflectivity is observed or simulated.

The pseudo-profiles computed with the procedure introduced above, are then used as observations in the RAMS-3DVar data assimilation (Federico, 2013), minimising the cost-function:

$$J(\mathbf{x}) = \frac{1}{2}(\mathbf{x} - \mathbf{x}_b)^T \mathbf{B}^{-1}(\mathbf{x} - \mathbf{x}_b) + \frac{1}{2}(\mathbf{z}_o^p - h(\mathbf{x}))^T \mathbf{R}^{-1}(\mathbf{z}_o^p - h(\mathbf{x}))$$

(4)

Where $\mathbf{x}$ is the state vector giving the analysis when J is minimized, $\mathbf{x}_b$ is the background, $\mathbf{B}$ and $\mathbf{R}$ are the background and observations error matrices, $\mathbf{z}_o^p$ is the pseudo vertical profile computed by Eqn. (2) and h is the forward observation operator transforming the state vector (RAMS@ISAC water vapour mixing ratio) into observations. The cost function in RAMS-3DVar is implemented in incremental form (Courtier et al., 1994) and its minimization is performed by the conjugate-gradient method (Press et al., 1992). No multi-scale approach is used.

The background error matrix is divided into three components along the three spatial directions (x, y, z). The $\mathbf{B}_x$ and $\mathbf{B}_y$ matrices account for the spatial correlation of the background error. The correlations are Gaussian with length-scales between 14 and 25 km, depending on the vertical level. These distances are computed using the NMC method (Barker et al., 2012) applied to the HyMeX-SOP1 (Hydrological cycle in the Mediterranean Experiment – First Special Observing Period occurred in the period 6 September-6 November 2012; Ducroq et al., 2014) period. It is again stressed that the spread of the innovations along the horizontal spatial directions in the 3D-Var analysis is determined by the length scales of $\mathbf{B}_x$ and $\mathbf{B}_y$ matrices and varies between 14 and 25 km, depending on the level.

The $\mathbf{B}_z$ matrix contains the error for the water vapour mixing ratio, which is the control variable used in RAMS-3DVar. This error is about 2 g/kg at the surface and decreases with height. In particular, it is larger than 0.5 g/kg below 4 km, and less than 0.2 g/kg above 5 km. The vertical decorrelation of the background error depends on the level and can be roughly estimated in 500-2000 m. The observation error matrix $\mathbf{R}$ in Eqn. (4) is diagonal and observations' errors are uncorrelated. This choice is partially justified by under sampling the radar reflectivity factor observation by choosing one point every five grid points in both horizontal directions of the radar

476 Cartesian grid. However, correlation observations errors have significant impact on the final
477 analysis, as shown for example in Stewart et al. (2013), and different choices of the matrix **R** will
478 be considered in future studies.

479 The value of the elements on the diagonal of **R** depends on the vertical level and are 1/4 of the
480 diagonal element of the **B$_z$** matrix at the corresponding height. By this choice, we give more credit
481 to the observations than to the background and analyses strongly adjust the background towards
482 observations.The background error matrix is computed using the NMC method (Parrish and
483 Derber, 1992; Barker et al. 2004) applied to the HyMeX-SOP1 (Hydrological cycle in the
484 Mediterranean Experiment – First Special Observing Period occurred from 6 September to6
485 November 2012; Ducroq et al., 2014). This choice is motivated by the fact that HyMeX-SOP1
486 contains several heavy precipitation events over Italy and the background error matrix is
487 representative of the convective environment of the cases considered in this paper. In particular,
488 10 out of 20 declared IOP (Intense Observing Period) of HyMeX-SOP1 occurred in Italy (Ferretti et
489 al., 2014). On the contrary, the period of September 2017, especially before the events selected in
490 this study was characterized by fair and stable weather conditions over Italy and the background
491 error matrix for September 2017 is less representative of the convective environment that
492 characterise the events of this paper.

493 Because it is the first time that we show the assimilation of radar reflectivity factor in
494 RAMS@ISAC, it is useful to discuss an example of analysis. We select the analysis of Livorno case
495 study at 06 UTC. The observed CAPPI at 3km above sea level is shown in Figure 10b. The
496 corresponding CAPPI simulated by the background is shown in Figure 14a. In general, the
497 comparison between simulated and observed reflectivity factor shows the difficulty of the model
498 to represent convection properly. In particular, the model is able to represent the convection over
499 Northern Italy but it has poor performance over Sardinia, south of Sicily and over Central Italy. The
500 difference between the analysis and background relative humidity after and before the analysis is
501 shown in Figure 14b (absolute values less than 1% are suppressed in the figure for clarity). Both
502 positive (convection enhancing) and negative (convection suppressing) adjustments are found.
503 Over Central Italy, Sardinia and South of Sicily relative humidity is increased because the model
504 doesn't simulate the observed reflectivity (Figure 10b). Over northern Italy the model is partially
505 dried for two different reasons: over northwest of Italy because RAMS@ISAC simulates
506 unobserved reflectivity, over north and northeast of Italy because the model simulates larger
507 values of reflectivity factor compared to the observations. The RAMS-3DVar is able to dry the

508 relative humidity field north of Corsica island, where the RAMS@ISAC predicts unobserved
509 reflectivity, while RAMS-3DVar didn't suppress the unobserved convection west of Sardinia
510 because the pseudo profiles computed over this area weren't appreciably drier than the
511 background.

512 Cross correlations among different variables of the data assimilation system are neglected in this
513 study and the application of the RAMS-3DVar affects the water vapour mixing ratio only. Cross
514 correlations among different variables can improve the performance of data assimilation system,
515 and an example of their impact in the RAMS-3DVar is shown in Federico (2013). Nevertheless, the
516 impact of cross correlations among different variables in the precipitation VSF will be explored in
517 future works.

518 Because also lightning data assimilation adjusts the water vapour mixing ratio, it follows that the
519 data assimilation presented in this study adjusts only this parameter.

520 Lightning and radar data assimilation may produce sharp gradients in vertical direction caused by
521 the addition of water vapour to specific layers. In the case of lightning, the water vapour is added
522 by nudging to reduce sharp gradients. However, radar data assimilation, which accounts for the
523 largest mass of water added to RAMS@ISAC (see Section S.1 of the supplemental material),
524 directly adjusts the water vapour into the model. Our experience with RAMS@ISAC, however,
525 shows that results are reliable and the sudden addition of water vapour doesn't cause shocks to
526 the model simulation, despite the notable gradients of specific humidity.

527 It is finally noted that the data assimilation increase/decrease the water vapour into the model
528 depending on the cases. The eventual increase/decrease of the forecasted rainfall depends on the
529 physical and dynamical processes occurring into the meteorological model, without any specific
530 tuning.

531

532 **4. Results**

533 In this section, we discuss the most intense phase of the Serano case, 03-06 UTC on 16 September,
534 and two VSF forecasts, 00-03 UTC and 06-09 UTC on 10 September, for the Livorno case. The two
535 VSF for Livorno correspond to the most intense phase of the storm in Livorno and to a very intense
536 phase over Lazio region, Central Italy. The aim of the section is to show the notable improvement
537 given by the lightning and radar reflectivity factor data assimilation to the VSF.

538 We consider four types of VSF (Table 3): a) CTRL, without radar reflectivity factor and lightning
539 data assimilation; b) LIGHT, assimilating lightning but not radar reflectivity factor; c) RAD,

assimilating radar reflectivity factor but not lightning; d) RADLI, assimilating both lightning and radar reflectivity factor.

In order to avoid excessive length two specific topics are considered in the supplemental material of this paper; specifically, we study: a) the relative contribution to the total water mass given by lightning and radar reflectivity factor data assimilation (Section S.1); b) the sensitivity of the precipitation VSF to the nudging formulation (Section S2). Also, the supplemental material gives different plots of Figures 15-17 (Section S3) and the forward radar operator used in RAMS-3DVar (Section S4).

4.1 Serano: 03-06 UTC on 16 September 2017

In this period, an intense and localised storm hit central Italy, while light precipitation occurred over northern Italy (Figure 15a). Considering the storm over central Italy, 10 raingauges observed more than 30 mm/3h, 6 more than 40 mm/3h, 3 more than 50 mm/3h and 1 more than 60 mm/3h, the maximum observed value being 63 mm/3h.

The CTRL forecast, Figure 15b, misses the storm over central Italy and considerably underestimates the precipitation area over Northern Italy, giving unsatisfactory results.

The assimilation of the radar reflectivity factor improves the forecast, as shown in Figure 15c. In particular, RAD forecast shows localized precipitation (30-35 mm/3h) close to the area were the most abundant precipitation was observed. However, the maximum precipitation is underestimated. Also, the RAD forecast better represents the precipitation over Northern Italy compared to CTRL.

The rainfall forecast of LIGHT, Figure 15d, shows some improvements compared to CTRL because the precipitation over central Italy has a maximum of 25-30 mm/3h, close to the area where the maximum precipitation was observed. LIGHT, however, has a worse performance compared to RAD because it underestimated the precipitation area over northern Italy. Also, similarly to RAD, LIGHT underestimates the maximum precipitation in central Italy.

RADLI forecast, Figure 15e, has the best performance. The precipitation over central Italy is well represented because the maximum rainfall (40-45 mm/3h) is in reasonable agreement with observations, and also because the area of intense precipitation (> 25 mm/3h) is elongated in the SW-NE direction in agreement with raingauge observations, giving a much better idea of the real storm intensity compared to RAD and LIGHT, as well as CTRL. The precipitation over northern Italy is well represented by RADLI.

572 Table 4 shows the ETS and POD scores for selected rainfall thresholds for different neighbourhood

573 radii. Different radii are considered to account for the well-known double penalty error (Mass et

574 al., 2002; Mittermaier et al., 2013) caused by displacement errors of the detailed precipitation

575 forecast in convection allowing grids. CTRL was unable to predict rainfall larger than 6 mm/3h. The

576 comparison between RAD and LIGHT shows that assimilating radar reflectivity factor performs

577 better than assimilating lightning. This behaviour, however, is not general and sometimes the

578 assimilation of lightning has a better performance than assimilating radar reflectivity factor (see

579 section 4.2.1).

580 RADLI forecast has the best performance among all model configurations. In particular, it is the

581 only forecast having positive scores for thresholds larger than 30 mm/3h.

582 In conclusion, for this VSF, the assimilation of lightning and radar reflectivity factor acted

583 synergistically to improve the precipitation VSF and the simulation assimilating both data performs

584 considerably better than simulations assimilating either lightning or radar reflectivity factor.

585

586 *4.2 Livorno*

587 The Livorno case study lasted for several hours starting at 18 UTC on 9 September 2017 and

588 ending more than a day later. The most intense phase in Livorno and its surroundings was

589 observed during the night between 9 and 10 September. In the following, we will show two

590 representative VSF (3h), including the most intense phase in Livorno.

591

592 *4.2.1 Livorno: 00-03 UTC on 10 September 2017*

593 This period represents the most intense phase of the storm in Livorno. In particular, the raingauge

594 close to the label A (Figure 16a) reported 151 mm/3h (Collesalvetti), while the one close to the

595 label B measured 82 mm/3h. Among the 518 raingauges reporting valid data, 75 observed more

596 than 10 mm/3h, 31 more than 20 mm/3h, 17 more than 30 mm/3h, 9 more than 40 mm/3h, and 6

597 more than 50 mm/3h.

598 The CTRL precipitation forecast is shown in Figure 16b. The forecast is poor because it misses the

599 precipitation swath from the coast towards NE. A precipitation swath is forecasted about 50 km to

600 the North of the real occurrence, but it is less wide compared to the observations.

601 The RAD forecast , Figure 16c, shows that the assimilation of radar reflectivity factor gives a clear

602 improvement to the forecast. The largest precipitation in the coastal part of the swath (we

603 searched for the maximum in the area with longitudes between 10.20E and 10.70E and latitudes

between 43.10N and 43.60N) is 94 mm/3h. Another local maximum is in the southern part of the domain (label B of Figure 16a). The maximum location is well represented, but the forecast value (55 mm/3h) underestimates the observed maximum (82 mm/3h).

An improvement, compared to both CTRL and RAD, is given by the assimilation of lightning (Figure 16d). Also for this simulation there is a precipitation swath from coastal Tuscany to the Apennines, but the shape of the swath better resembles that observed. The maximum value close to Livorno, i.e. in the coastal part of the swath, is 158 mm/3h.

LIGHT simulation shows the local maximum in the southern part of the domain (about 50 mm/3h), but the amount is underestimated.

Figure 16e shows the RADLI rainfall forecast. The precipitation swath from coastal Tuscany towards NE is more apparent compared to LIGHT and RAD. The maximum rainfall accumulated close to Livorno is 186 mm/3h. Also, the second precipitation maximum in the southern part of the domain reaches 70 mm/3h in good agreement with observations (82 mm/3h). RADLI is the only run giving a satisfactory precipitation VSF over the south-eastern Emilia Romagna (north-eastern part of the domain), to the lee of the Apennines. It is also noted that the main precipitation swath forecasted by RADLI is too broad in the direction crossing the swath compared to the observations. This is confirmed by the FBIAS of RADLI (not shown), which is more than 3 for thresholds larger than 42 mm/3h.

The analysis of the scores (Table 5) confirms the results outlined above. CTRL has the lowest performance and the improvement given by the data assimilation to the VSF is apparent for POD and ETS for all thresholds and neighbourhood radii considered. For this specific VSF, lightning data assimilation gives a better improvement to rainfall forecast compared to RAD. RADLI has the best performance, especially for 25 km and 50 km neighbourhood radii, nevertheless it over forecast the precipitation field. Because ETS penalises false alarms, the value of this score for RADLI is sometimes lower than that of LIGHT.

4.2.3 Livorno: 06-09 UTC on 10 September 2017

In this period, the most intense precipitation occurred over the coastal part of Lazio (Figure 17a). More in detail, among the 2695 raingauges reporting valid data over the domain of Figure 17a, 307 reported more than 10 mm/3h, 132 more than 20 mm/3h, 86 more than 30 mm/3h, 66 more than 40 mm/3h, 49 more than 50 mm/3h and 35 more than 60 mm/3h. Among the 35 raingauges

635   measuring more than 60 mm/3h, 33 were over Lazio, showing the heavy rainfall occurred over the

636   Region.

637   Some precipitation persisted over Tuscany but the rainfall is much lower compared to previous 6h

638   (the rainfall over Tuscany between 03 and 06 UTC was very intense, not shown). Other notable

639   precipitation areas are over the NE of Italy (moderate to low amounts), over central Alps

640   (moderate values) and over the whole Sardinia (small amounts).

641   Figure 17b shows the rainfall simulated by CTRL. The forecast is unsatisfactory, mainly for the

642   following two reasons: a) heavy precipitation is simulated over Tuscany (> 75 mm/3h), also close

643   to the Livorno area; b) few millimetres of precipitation are forecasted over central Italy. The

644   rainfall over NE Italy is well represented in space, but overestimated.

645   Considering the evolution of CTRL forecast for the two VSF of Livorno, we conclude that it was

646   able to predict abundant rain over Livorno, but the rainfall forecast was delayed compared to the

647   real occurrence. A similar behaviour was found in Ricciardelli et al. (2018) using the WRF model,

648   showing that the results of this paper for Livorno are likely not tied to the specific model used.

649   The rainfall simulated by RAD (Figure 17c) clearly improves the forecast compared to CTRL. First,

650   the precipitation over Lazio is very well predicted and the rainfall values are up to 65 mm/3h, so

651   RAD forecast well represents the main precipitation spot over Italy for this VSF. Second, the

652   precipitation over Tuscany is less than for CTRL, showing the ability of radar reflectivity factor data

653   assimilation to dry the model when it predicts reflectivity that is not observed. This is confirmed

654   by the inspection of the analysis of Figure 14b, the last analysis used before this VSF, which gives a

655   decrease of the relative humidity over most of Tuscany and over the sea in front of Livorno. Third,

656   the precipitation over central Alps is represented, even if located about 30 km to the East. It is

657   noted, however, that the area of intense rainfall (>60 mm/3h) is overestimated by RAD, showing a

658   wet forecast. This is confirmed by the wet frequency bias of the RAD simulation, which is greater

659   than 3 between 14 and 44 mm/3h. The wet bias of the RAD forecast is apparent in the

660   representation of the rainfall VSF shown in the supplemental material of this paper (Figure S5).

661   LIGHT forecast, Figure 17d, shows a worse performance compared to RAD for this time period. The

662   precipitation forecast is mainly over Tuscany, where it is overestimated, with a small precipitation

663   spot over Lazio.

664   The precipitation forecast of RADLI, Figure 17e, represents very well the precipitation over Lazio,

665   and the rainfall amount is better predicted compared to RAD. The precipitation over Sardinia is

666 well represented by RADLI as well as the precipitation over Central Alps, giving the best results
667 among all VSF.

668 The analysis of the scores confirms the above results (Table 6). CTRL has a poor performance as
669 shown by the POD and ETS values, close to zero, for all thresholds above 30 mm/3h and for all
670 neighbourhood radii. The simulations assimilating radar reflectivity factor performs better than
671 LIGHT, the difference being larger for higher rainfall thresholds and for smaller neighbourhood
672 radii.

673 It is also notable the good performance of RADLI forecast for the nearest neighbourhood radii
674 (ETS=0.43, POD=0.92) for the 50 mm/3h threshold.

675

676 **5. Discussion and Conclusions**

677 In this paper, we showed the impact of lightning and radar reflectivity factor data assimilation on
678 the very short term precipitation forecast (3h) for two case studies occurred in Italy. We used
679 RAMS@ISAC model, whose 3DVar extension to the assimilation of radar reflectivity factor is
680 shown in this paper for the first time.

681 The first case study occurred on 16 September 2017 and it is a moderate case with localised
682 rainfall over central Italy. It was chosen because the control forecast, i.e. without radar reflectivity
683 factor or lightning data assimilation, missed the event. The second event, occurred on 9-10
684 September 2017, was characterised by exceptional rainfall over several parts of Italy. This event
685 was partially represented by the control forecast. In particular, the forecast of the event was
686 incorrect because: a) the control forecast was delayed compared to the observations; b) the
687 control forecast missed the rainfall over central Italy (Lazio Region).

688 It is important to recall that the impact of the lightning data assimilation on the precipitation
689 forecast of RAMS@ISAC was already studied for the HyMeX-SOP1 period (Federico et al., 2017a,
690 2017b), and a robust statistic is already available. The results of this study confirm the important
691 role of the lightning data assimilation on the rainfall forecast for other two case studies. However,
692 considering the assimilation of radar reflectivity factor, and its combination with lightning data
693 assimilation in RAMS@ISAC, the results of this paper are new.

694 Because we analysed only two case studies, no definitive conclusions can be derived on the
695 performance of RAMS@ISAC for radar reflectivity factor data assimilation. There are, however,
696 few points worth of mention.

The VSF performance of RAMS@ISAC is systematically improved by the assimilation of radar reflectivity factor. This improvement is of paramount importance for some specific VSF (for example for the 00-03 UTC of Livorno), when the control forecast missed the event while it was correctly predicted by radar reflectivity factor data assimilation. Sometimes the improvement of reflectivity factor data assimilation has a lower impact on the precipitation forecast, as for the period 18-21 UTC on 9 September 2017 (Livorno, not shown, see the discussion paper Federico et al. (2018) for a description of this VSF). This suggests that there is space for improvement for all components of the VSF: observations, data assimilation, meteorological model.

Lightning and radar observations are different and both add value to the VSF. In particular, flashes are recorded when deep convection develops, while radar reflectivity factor is observed also for light stratiform rain. Flashes of ground based network, as LINET, are available over the open sea, even if with a reduced detection efficiency, while radar reflectivity factor is confined to the range of coastal radars in the network. Lightning has a seasonal dependence over Italy, with the maximum in summer and fall, while radar reflectivity factor is available in all seasons.

For the above reasons, the impact of the two kinds of data on the rainfall VSF is expected different. Some examples have been shown: the light precipitation over Northern Italy for Serano is well forecasted assimilating radar reflectivity factor, while it is not simulated assimilating flashes because they are too few in this area to force convection; lightning data assimilation is able to better represent the deep convection occurring during the intense phase of the Livorno case (00-03 UTC), especially because it is able to force convection where it occurs, reducing false alarms. The ability of lightning data assimilation to reduce false alarms compared to RAD and RADLI it is shown by the fact that the ETS score for LIGHT is sometimes the best among all simulations (see also the section S2 of the supplemental material of this paper). These results show also that the influence of different observations depends on the meteorological situation.

The model configuration assimilating both radar reflectivity factor and lightning (RADLI) is able to retain important features of both data assimilation. For example, the simulation of the Livorno case in the phase 06-09 UTC was able to simulate the heavy precipitation over Lazio thanks to the radar reflectivity factor data assimilation and the precipitation over Sardinia, as well as the moderate precipitation over central Alps, thanks to lightning data assimilation.

The property of RADLI to retain the precipitation features of both RAD and LIGHT it is shown by the POD score, which is the best, for most cases and thresholds, for RADLI.

728   Another interesting feature is the considerable improvement of the POD of RADLI compared to

729   CTRL for the lowest thresholds.

730   It is also underlined that the data assimilated, both lightning and radar reflectivity factor, are

731   available in real time and could be used for an operational implementation of the VSF.

732   All the above features are promising and deserve future studies to better understand the role of

733   radar reflectivity factor and its interaction with lightning data assimilation to improve the

734   precipitation forecast.

735   There are, however, less satisfactory aspects of assimilating both radar reflectivity factor and

736   lightning data. In particular, the wet bias of RAD and RADLI forecast is the main drawback of the

737   results of this paper. To reduce the moisture added by radar and lightning data assimilation

738   further research is needed and different approaches are possible (Fierro et al., 2016). In particular:

739   a) assimilating for a shorter time (0-6h in this paper); b) reducing the length-scales of the 3D-Var in

740   the horizontal directions to limit the spreading of the innovations, or assuming an innovation

741   equal to zero for grid points without lightning and with zero reflectivity factor; c) reducing the

742   amount of water vapour added to the model (for example reducing the values of A and B

743   constants for lightning data assimilation or relaxing the request of saturation when radar

744   reflectivity is observed in areas where the model has zero reflectivity); d) adding moisture to a

745   shallower vertical layer.

746   It is also noted that a combination of heating and moistening could provide the same buoyancy

747   with less water vapour addition (Marchand and Fulberg, 2014) and this approach could be used in

748   future studies.

749   In addition to the acquisition of more case studies, there are two directions of future development

750   of this work. The lightning data assimilation can be formulated by 3DVar, using a strategy similar

751   to the radar reflectivity factor in which pseudo-profiles of relative humidity are first generated

752   where flashes are recorded, and then those profiles are assimilated by 3DVar. This methodology

753   was already reported in Fierro et al. (2016). The assimilation of both radar reflectivity factor and

754   lightning using RAMS-3DVar will be explored in future studies.

755   Another important point to study is how long the innovations introduced by data assimilation lasts

756   in the forecast. While in this study we consider the VSF at 3h, future studies must explore longer

757   time ranges. This kind of study was performed for lightning data assimilation (Fierro et al., (2015);

758   Federico et al., 2017b; Lynn et al. (2015) among others) and for radar data assimilation (Hu et al.

759   (2006); Jones et al. (2014), among others), using a rationale similar to that used in this paper.

In general, the performance of the forecast and the impact of lightning and radar data assimilation decrease with forecasting time because of the propagation of boundary conditions inside the domain and because of model errors growth. Improving the data assimilation system also contributes to a longer resilience of model performance. The studies cited above showed that lightning and radar data assimilation can have an impact up to 24h depending on several factors (meteorological model, data assimilation, quality of the data, meteorological conditions, initial and boundary conditions).

A study considering both radar reflectivity factor and lightning should be performed to understand the resilience of the innovations introduced by data assimilation.

ACKNOWLEDGMENTS

This work is a contribution to the HyMeX program. Part of the computational time used for this paper was granted by the ECMWF (European Centre for Medium Weather range Forecast) thoughout the special project SPITFEDE. LINET data were provided by Nowcast GmbH (https://www.nowcast.de/) within a scientific agreement between H.D. Betz and the Satellite Meteorological Group of CNR-ISAC in Rome.

This work was partially funded by the agreement between CNR-ISAC and the Italian Department of Civil Protection.

References

Alexander, G. D., Weinman, J. A., Karyampoudi, V. M., Olson, W. S., and Lee, A. C. L.: The effect of assimilating rain rates derived from satellites and lightning on forecasts of the 1993 superstorm, Mon. Weather Rev., 127, 1433–1457, 1999.

Barker, D.M., Huang, W., Guo, Y.-R., and Xiao, Q.N.: A Three-Dimensional Variational Data Assimilation System for MM5: Implementation And Initial Results, Monthly Weather Review, 132, 897-914, 2004.

Barker, D. M., Huang, X.-Y., Liu, Z., Auligné, T., Zhang, X., Rugg ,S., Ajjaji, R., Bourgeois, A., Bray, J., Chen ,Y., Demirtas, M.,. Guo, Y.-R, Henderson, T., Huang, W, Lin, H.C., Michalakes, J., Rizvi, S., and Zhang, X.: The Weather Research and Forecasting (WRF) Model's Community Variational/Ensemble Data Assimilation System: WRFDA. Bull. Amer. Meteor. Soc., 93, 831–843, 2012.

793   Betz, H.-D., Schmidt, K., Laroche, P., Blanchet, P., Oettinger, P., Defer, E., Dziewit, Z., and Konarski,
794   J.: LINET-an international lightning detection network in Europe, Atmos. Res., 91, 564– 573, 2009.

795   Buzzi, A. and Tibaldi, S.: Cyclogenesis in the lee of the Alps: A case study. Q.J.R. Meteorol. Soc.,
796   104: 271-287. https://doi.org/10.1002/qj.49710444004, 1978.

797   Caumont, O., Ducrocq, V., Wattrelot, E., Jaubert, G., and Pradier-Vabre, S.: 1D+3DVar assimilation
798   of radar reflectivity data: a proof of concept, Tellus A: Dynamic Meteorology and
799   Oceanography, 62:2, 173-187, https://www.tandfonline.com/doi/abs/10.1111/j.1600-
800   0870.2009.00430.x, 2010.

801   Carey, L. D., and S. A. Rutledge: Electrical and multiparameter radar observations of a severe
802   hailstorm. J. Geophys. Res., 103, 13 979–14 000, doi:10.1029/97JD02626, 1998.

803   Chang, D. E., Weinman, J. A., Morales, C. A., and Olson, W. S.: The effect of spaceborn microwave
804   and ground-based continuous lightning measurements on forecasts of the 1998 Groundhog Day
805   storm, Mon. Weather Rev., 129, 1809–1833, 2001.

806   Chen, C. and Cotton, W.R.: A One-Dimensional Simulation of the Stratocumulus-Capped Mixed
807   Layer, Boundary Layer Meteorology, 25, 289-321, 1983.

808   Cotton, W.R., Pielke Sr., R.A., Walko, R.L., Liston, G.E., Tremback, C.J., Jiang, H., McAnelly, R.L.,
809   Harrington, J.Y.m Nicholls, M.E., Carrio, G.G., and McFadden, J.P.: RAMS 2001: Current status and
810   future directions, Meteorology and Atmospheric Physics, 82, 5-29,2003.

811   Courtier, P., Thépaut, J. N., and Hollingsworth, A.: A strategy for operational implementation of
812   4D-Var, using an incremental approach, Q. J. Roy. Meteorol. Soc., 120, 1367–1387, 1994.

813   Dahl, J. M. L., Höller, H., and Schumann, U.: Modeling the Flash Rate of Thunderstorms. Part II:
814   Implementation. Monthly Weather Review, 139, 3112-3124, 2011.

815   Deierling, W., and W. A. Peterse: Total lightning activity as an indicator of updraft characteristics. J.
816   Geophys. Res., 113, D16210, doi:10.1029/2007JD009598, 2008.

817   Ducrocq, V., Braud, I., Davolio, S., Ferretti, R., Flamant, C., Jansa, A., Kalthoff, N., Richard, E.,
818   Taupier-Letage, I., Ayral, P.-A., Belamari, S., Berne, A., Borga, M., Boudevillain, B., Bock, O.,
819   Boichard, J.-L., Bouin, M.-N., Bousquet, O., Bouvier, C., Chiggiato, J., Cimini, D., Corsmeier, U.,
820   Coppola, L., Cocquerez, P., Defer, E., Delanoë, J., Di Girolamo, P., Doerenbecher, A., Drobinski, P.,
821   Dufournet, Y., Fourrié, N., Gourley, J.J., Labatut, L., Lambert, D., Le Coz, J., Marzano, F.S., Molinié,
822   G., Montani, A., Nord, G., Nuret, M., Ramage, K., Rison, W., Roussot, O., Said, F., Schwarzenboeck,
823   A., Testor, P., Van Baelen, J., Vincendon, B., Aran, M., and Tamayo, J.: HYMEX-SOP1 The Field
824   Campaign Dedicated to Heavy Precipitation and Flash Flooding in the Northwestern
825   Mediterranean. Bull. Amer. Meteor. Soc., 95, 1083–1100, https://doi.org/10.1175/BAMS-D-12-
826   00244.1 , 2014.

827 Emersic, C., and C. P. R. Saunders, 2010: Further laboratory investigations into the relative
828 diffusional growth rate theory of thunderstorm electrification. Atmos. Res., 98, 327–340,
829 doi:https://doi.org/10.1016/j.atmosres.2010.07.011, 2010.

830 Fabry, F., and Sun, J: For how long should what data be assimilated for the mesoscale forecasting
831 of convection and why? Part I: On the propagation of initial condition errors and their implications
832 for data assimilation. Monthly Weather Review, 138(1), 242–255, https://doi.org
833 /2009mwr2883.1, 2010.

834 Federico, S.: Implementation of a 3D-Var system for atmospheric profiling data assimilation into
835 the RAMS model: Initial results, Atmospheric Measurement Techniques, 6(12), 3563-3576, 2013.

836 Federico, S.: Implementation of the WSM5 and WSM6 Single Moment Microphysics Scheme into
837 the RAMS Model: Verification for the HyMeX-SOP1, Advances in Meteorology, Volume 2016,
838 2016.

839 Federico, S., Avolio, E., Petracca, M., Panegrossi, G., Sanò, P., Casella, D., and Dietrich S.:Simulating
840 lightning into the RAMS model: Implementation and preliminary results, Natural Hazards and
841 Earth System Sciences, Volume 14, Number 11, p.2933-2950, 2014.

842 Federico, S., Petracca, M., Panegrossi, G., and Dietrich, S.: Improvement of RAMS precipitation
843 forecast at the short-range through lightning data assimilation, Nat. Hazards Earth Syst. Sci., 17,
844 61–76, https://doi.org/10.5194/nhess-17-61-2017, 2017a.

845 Federico, S., Petracca, M., Panegrossi, G., Transerici, C., and Dietrich, S.: Impact of the assimilation
846 of lightning data on the precipitation forecast at different forecast ranges. Adv. Sci. Res., 14, 187–
847 194, 2017b.

848 Federico, S., Torcasio, R. C., Avolio, E., Caumont, O., Montopoli, M., Baldini, L., Vulpiani, G., and
849 Dietrich, S.: The impact of lightning and radar data assimilation on the performance of very short
850 term rainfall forecast for two case studies in Italy, Nat. Hazards Earth Syst. Sci. Discuss.,
851 https://doi.org/10.5194/nhess-2018-319, in review, 2018.

852 Ferretti, R., Pichelli, E., Gentile, S., Maiello, I., Cimini, D., Davolio, S., Miglietta, M. M., Panegrossi,
853 G., Baldini, L., Pasi, F., Marzano, F. S., Zinzi, A., Mariani, S., Casaioli, M., Bartolini, G., Loglisci, N.,
854 Montani, A., Marsigli, C., Manzato, A., Pucillo, A., Ferrario, M. E., Colaiuda, V., and Rotunno, R.:
855 Overview of the first HyMeX Special Observation Period over Italy: observations and model
856 results, Hydrol. Earth Syst. Sci., 18, 1953–1977, https://doi.org/10.5194/hess-18-1953-2014, 2014.

857 Fierro, A. O., A. J. Clark, E. R. Mansell, D. R. MacGorman, S. Dembek, and C. Ziegler: Impact of
858 storm-scale lightning data assimilation on WRF-ARW precipitation forecasts during the 2013 warm
859 season over the contiguous United States. Mon. Wea. Rev., 143, 757–777,
860 doi:https://doi.org/10.1175/MWR-D-14-00183.1, 2015.

861 Fierro, A.O., Gao, l., Ziegler, C. L., Calhoun, K. M., Mansell, E. R., and MacGorman, D.
862 R.: Assimilation of Flash Extent Data in the Variational Framework at Convection-Allowing Scales:
863 Proof-of-Concept and Evaluation for the Short-Term Forecast of the 24 May 2011 Tornado
864 Outbreak. Mon. Wea. Rev., 144, 4373–4393,https://doi.org/10.1175/MWR-D-16-0053.1, 2016.

865 Fierro, A. O., J. Gao, C. Ziegler, E. R. Mansell, D. R. MacGorman, and S. Dembek: Evaluation of a
866 cloud scale lightning data assimilation technique and a 3DVAR method for the analysis and short-
867 term forecast of the 29 June 2012 derecho event. Mon. Wea. Rev., 142, 183–202, doi:10.1175/
868 MWR-D-13-00142.1, 2014.

869 Fierro, A. O., M. S. Gilmore, E. R. Mansell, L. J. Wicker, and J. M. Straka: Electrification and lightning
870 in an idealized boundary-crossing supercell simulation of 2 June 1995. Mon. Wea. Rev., 134, 3149–
871 3172, doi:10.1175/MWR3231.1, 2006.

872 Fierro, A. O., Mansell, E., Ziegler, C., and MacGorman, D.: Application of a lightning data
873 assimilation technique in the WRFARW model at cloud-resolving scales for the tornado outbreak
874 of 24 May 2011, Mon. Weather Rev., 140, 2609–2627, 2012.

875 Giannaros, T. M., Kotroni, V., and Lagouvardos, K.: WRFLTNGDA: A lightning data assimilation
876 technique implemented in the WRF model for improving precipitation forecasts, Environ. Model.
877 Softw., 76, 54–68, doi:10.1016/j.envsoft.2015.11.017, 2016.

878 Hong, S.Y., Lim, J.J.O.: The WRF single-moment 6-class microphysics scheme (WSM6). J. Korean
879 Meteorol. Soc. 42, 129–151, 2006.

880 Hu, M., M. Xue, and K. Brewster: 3DVAR and cloud analysis with WSR-88D level-II data for the
881 prediction of the Fort Worth, Texas, tornadic thunderstorms. Part I: Cloud analysis and its impact.
882 Mon. Wea. Rev., 134, 675–698, doi:10.1175/MWR3092.1, 2006.

883 Ikuta, Y. and Honda, Y.: Development of 1D+4DVAR data assimilation of radar reflectivity in JNoVA.
884 Tech. Report, 01.09–01.10. http://www.wcrp-climate.org/WGNE/BlueBook/2011/individual-
885 articles/01_Ikuta_Yasutaka_WGNE2011_1D4DVAR.pdf, 2011.

886 Jones, C. D., and Macpherson, B.: A latent heat nudging scheme for the assimilation of
887 precipitation into an operational mesoscale model, Meteorol. Appl., 4, 269–277, 1997.

888 Jones, T. A., J. A. Otkin, D. J. Stensrud, and K. Knopfmeier: Forecast evaluation of an observing
889 system simulation experiment assimilating both radar and satellite data. Mon. Wea. Rev., 142,
890 107–124, doi:10.1175/MWR-D-13-00151.1, 2014.

891 Kain, J. S. and Fritsch, J. M.: Convective parameterization for mesoscale models: the Kain-Fritsch
892 scheme. The representation of cumulus convection in numerical models, Meteor. Monogr. No. 46,
893 Am. Meteor. Soc., Boston, 165–170, 1993.

894 Kuhlman, K. M., C. L. Zielger, E. R. Mansell, D. R. MacGorman, and J. M. Straka: Numerically
895 simulated electrification and lightning of the 29 June 2000 STEPS supercell storm. Mon. Wea. Rev.,
896 134, 2734–2757, doi:10.1175/MWR3217.1, 2006.

897 Kummerow, C., Hong, Y., Olson, W.S., Yang. S., Adler, R.F., McCollum, J., Ferraro, R., Petty, G., Shin.
898 D.-B., and Wilheit, T.T.: The evolution of the Goddard profiling algorithm (GPROF) for rainfall
899 estimation from passive microwave sensors. J. Appl. Meteor., 40, 1801–1820, 2001.

900 Lagouvardos, K., Kotroni, V., Betz, H.-D., and Schmidt, K.: A comparison of lightning data provided
901 by ZEUS and LINET networks over Western Europe, Nat. Hazards Earth Syst. Sci., 9, 1713–1717,
902 https://doi.org/10.5194/nhess-9-1713-2009, 2009.

903 Lynn, B. H., G. Kelman, and G. Ellrod: An evaluation of the efficacy of using observed lightning to
904 improve convective lightning forecasts. Wea. Forecasting, 30, 405-423 doi:10.1175/ WAF-D-13-
905 00028.1., 2015.

906 Lynn, B.H., 2017: The Usefulness and Economic Value of Total Lightning Forecasts Made with a
907 Dynamic Lightning Scheme Coupled with Lightning Data Assimilation.Wea. Forecasting, 32, 645–
908 663, https://doi.org/10.1175/WAF-D-16-0031.1 , 2017.

909 MacGorman, I. R. Apostolakopoulos, N. R. Lund, N. W. S. Demetriades, M. J. Murphy, and P. R.
910 Krehbiel: The timing of cloud-to-ground lightning relative to total lightning activity. Mon. Wea.
911 Rev., 139, 3871–3886, doi:10.1175/MWR-D-11-00047.1, 2011.

912 MacGorman, D. W. Burgess, V. Mazur, W. D. Rust, W. L. Taylor, and B. C. Johnson, 1989: Lightning
913 rates relative to tornadic storm evolution on 22 May 1981. J. Atmos. Sci., 46, 221–251,
914 doi:10.1175/ 1520-0469(1989)046,0221:LRRTTS.2.0.CO;2.

915 MacGorman, D.R. and K.E. Nielsen: Cloud-to-Ground Lightning in a Tornadic Storm on 8 May 1986.
916 Mon.   Wea.   Rev.,   119,   1557–1574,   https://doi.org/10.1175/1520-
917 0493(1991)119<1557:CTGLIA>2.0.CO;2, 1991.

918 MacGorman, W. D. Rust, P. Krehbiel, W. Rison, E. Bruning, and K. Wiens: The electrical structure of
919 two supercell storms during STEPS. Mon. Wea. Rev., 133, 2583–2607, doi:10.1175/MWR2994.1,
920 2005.

921 MacGorman, W. D. Rust, P. Krehbiel, W. Rison, E. Bruning, and K. Wiens: The electrical structure of
922 two supercell storms during STEPS. Mon. Wea. Rev., 133, 2583–2607, doi:10.1175/MWR2994.1,
923 2005.

924 Maiello, I., Ferretti, R., Gentile, S., Montopoli, M., Picciotti, E., Marzano, F. S., and Faccani, C.:
925 Impact of radar data assimilation for the simulation of a heavy rainfall case in central Italy using
926 WRF–3DVAR, Atmos. Meas. Tech., 7, 2919-2935, https://doi.org/10.5194/amt-7-2919-2014, 2014.

927 Mansell, E. R., Ziegler, C. L., and MacGorman, D. R.: A lightning data assimilation technique for
928 mesoscale forecast models, Mon. Weather Rev., 135, 1732–1748, 2007.

929 Marchand, M., and H. Fuelberg: Assimilation of lightning data using a nudging method involving
930 low-level warming. Mon. Wea. Rev., 142, 4850–4871, doi:10.1175/MWR-D-14-00076.1, 2014.
931

932 Mass, C. F., Ovens, D., Westrick, K., and Colle, B. A.: Does increasing horizontal resolution produce
933 more skilful forecasts?, B. Am. Meteorol. Soc., 83, 407–430, 2002.

934 Mellor, G., and Yamada, T.: Development of a Turbulence Closure Model for Geophysical Fluid
935 Problems, Review of Geophysics and Space Physics, 20, 851-875, 1982.

936 Mittermaier, M., N. Roberts, and S. A. Thompson: A long-term assessment of precipitation forecast
937 skill using the Fractions Skill Score. Meteor. Appl., 20, 176–186,
938 doi:https://doi.org/10.1002/met.296, 2013.

939 Molinari, J., and Corsetti, T.: Incorporation of cloud-scale and mesoscale down-drafts into a
940 cumulus parametrization: results of one and three-dimensional integrations, Monthly Weather
941 Review, 113, 485-501, 1985.

942 Olson, W. S., Kummerow, C. D. , Heymsfield, G. M., and Giglio, L.: A method for combined passive-
943 active microwave retrievals of cloud and precipitation profiles. J. Appl. Meteor., 35, 1763-1789,
944 1996.

945 Papadopoulos, A., Chronis, T.G., Anagnostou, E.N.. Improving convective precipitation forecasting
946 through assimilation of regional lightning measurements in a mesoscale model. Mon. Weather
947 Rev. 133, 1961-1977, 2005ì.

948 Parrish, D.F., and Derber, J.C.: The National Meteorological Center's Spectral Statistical
949 Interpolation analysis system, Monthly Weather Review, 120, 1747-1763, 1992.

950 Pessi, A.T. and S. Businger: Relationships among Lightning, Precipitation, and Hydrometeor
951 Characteristics over the North Pacific Ocean. J. Appl. Meteor. Climatol., 48, 833–
952 848, https://doi.org/10.1175/2008JAMC1817.1 , 2009.

953 Petracca M., Casella D., Dietrich S., Milani L., Panegrossi G., Sanò P., Möhrlein M., Riso S. and Betz
954 H.D. (2014), "Lightning strokes frequency homogenization for climatological analysis: application
955 to LINET data records over Europe", 2nd TEA – IS Summer School, June 23 – 27, Collioure, France,
956 2014.

957 Petracca, M., L. P. D'Adderio, F. Porcù, G. Vulpiani, S. Sebastianelli, and S. Puca: Validation of GPM
958 Dual-Frequency Precipitation Radar (DPR) rainfall products over Italy. J. Hydrometeor., 19, 907–
959 925. https://doi.org/10.1175/JHM-D-17-0144.1., 2018.

960 Press, W. H., Teukolsky, S. A., Vetterling, W. T., and Flannery, B. P.: Numerical recipes in Fortran
961 77, second ed., Cambridge Uni- versity Press, Cambridge, 992 pp., 1992.

962 Qie, X., Zhu, R., Yuan, T., Wu, X., Li, W., and Liu, D.: Application of total-lightning data assimilation
963 in a mesoscale convective system based on the WRF model, Atmos. Res., 145–146, 255–266, 2014.

964 Ricciardelli, E.; Di Paola, F.; Gentile, S.; Cersosimo, A.; Cimini, D.; Gallucci, D.; Geraldi, E.; Larosa, S.;
965 Nilo, S.T.; Ripepi, E.; Romano, F.; Viggiano, M. Analysis of Livorno Heavy Rainfall Event: Examples
966 of Satellite-Based Observation Techniques in Support of Numerical Weather Prediction. Remote
967 Sens. 2018, 10, 1549, 2018.

969 Ridal, M., and Dahlbom, M.: Assimilation of multinational radar reflectivity data in a mesoscale
970 model: a proof of concept, Journal of Applied Meteorology and Climatology, 56(6), 1739–1751,
971 https://doi.org/10.1175/jamc-d-16-0247.1, 2017.

972 Rohn, M., Kelly, G., Saunders, R. W.: Impact of a New Cloud Motion Wind Product from Meteosat
973 on NWP Analyses and Forecasts, Monthly Weather Review, 129, 2392-2403, 2001.

974 Skamarock, W. C., Klemp, J. B., Dudhia, J., Gill, D. O., Barker, D. M., Duda, M. G., Huang, X.-Y.,
975 Wang, W., and Powers, J. G.: A description of the Advanced Reasearch WRF Version 3. NCAR
976 Technical Note, TN 475+STR, 113 pp., available at:
977 http://www2.mmm.ucar.edu/wrf/users/docs/arw_v3.pdf (last access: November 2018), 2008.

978 Smagorinsky, J.: General circulation experiments with the primitive equations. Part I, The basic
979 experiment, Monthly Weather Review, 91, 99-164, 1963.

980 Stensrud, D. J., and Fritsch, J. M.: Mesoscale convective systems in weakly forced large-scale
981 environments. Part II: Generation of a mesoscale initial condition, Mon. Weather Rev., 122, 2068-
982 2083, 1994.

983 Stensrud, D.J., M. Xue, L.J. Wicker, K.E. Kelleher, M.P. Foster, J.T. Schaefer, R.S. Schneider, S.G.
984 Benjamin, S.S. Weygandt, J.T. Ferree, and J.P. Tuell: Convective-Scale Warn-on-Forecast System.
985 Bull. Amer. Meteor. Soc., 90, 1487–1500, https://doi.org/10.1175/2009BAMS2795.1, 2009.

986 Stewart, L. M., Dance, S. L., Nichols, N. K.: Data assimilation with correlated observation errors:
987 experiments with a 1-D shallow water model, Tellus A: Dynamic Meteorology and
988 Oceanography, 65:1, DOI: 10.3402/tellusa.v65i0.19546, 2013.

989 Sun, J., and Crook, N. A.: Dynamical and Microphysical Retrieval from Doppler RADAR
990 Observations Using a Cloud Model and Its Adjoint, Part I: Model Development and Simulated Data
991 Experiments, J. Atmos. Sci., 54, 1642–1661, 1997.

992 Sun, J., and Crook, N. A.: Dynamical and Microphysical Retrieval from Doppler RADAR
993 Observations Using a Cloud Model and Its Adjoint, Part II: Retrieval Experiments of an Observed
994 Florida Convective Storm, J. Atmos. Sci., 55, 835–852, 1998.

995 Sun, J. and Wang, H.: Radar data assimilation with WRF 4DVar. Part II: comparison with 3D-Var for
996 a squall line over the US Great Plains, Mon. Weather Rev., 11, 2245–2264,
997 https://doi.org/10.1175/MWR-D-12-00169.1, 2012.

998 Takahashi, T.: Riming electrification as a charge generation mechanism in thunderstorms. J.
999 Atmos. Sci., 35, 1536–1548, doi:https://doi.org/10.1175/1520 0469(1978)0352.0.CO;2, 1978.

Vulpiani, G., A. Rinollo, S. Puca, and M. Montopoli: A quality-based approach for radar rain field reconstruction and the H-SAF precipitation products validation. Proc. Eighth European Radar Conf., Garmish-Partenkirchen, Germany, ERAD, Abstract 220, 6 pp., http://www.pa.op.dlr.de/erad2014/programme/ ExtendedAbstracts/220_Vulpiani.pdf (last access January 2019), 2014.

Walko, R.L., Band, L.E., Baron, J., Kittel, T.G., Lammers, R., Lee, T.J., Ojima, D., Pielke Sr., R.A., Taylor, C., Tague, C., Tremback, C.J., and Vidale, P.L.: Coupled Atmosphere-Biosphere-Hydrology Models for environmental prediction, Journal of Applied Meteorology, 39, 931-944, 2000.

Wang, H., Sun, J., Zhang, X., Huang, X., and Auligne, T.: Radar data assimilation with WRF 4D-Var. Part I: system development and preliminary testing, Mon. Weather Rev., 141, 2224–2244, 2013.

Wattrelot, É., Caumont, O. and Mahfouf, J. F.: Operational implementation of the 1D+3D-Var assimilation method of radar reflectivity data in the AROME model. Monthly Weather Review, 142(5), 1852–1873. https://doi.org/10.1175/MWR-D-13-00230.1, 2014.

Weisman, M. L., Skamarock, W. C., and Klemp, J. B.: The resolution dependence of explicitly modeled convective systems, Mon.Weather Rev., 125, 527–548, 1997.

Weygandt, S. S., Benjamin, S. G., Hu, M., Smirnova, T. G., and Brown, J. M.: Use of lightning data to enhance radar assimilation within the RUC and Rapid Refresh models. Third Conf. on Meteorological Applications of Lightning Data, 20–24 January 2008, New Orleans, LA, Amer. Meteor. Soc., 8.4, available at: https://ams.confex.com/ams/88Annual/webprogram/Paper134112.html (last access: 03 October 2018), 2008.

Wiens, K. C., S. A. Rutledge, and S. A. Tessendorf, A: The 29 June 2000 supercell observed during STEPS. Part II: Lightning and charge structure. J. Atmos. Sci., 62, 4151–4177, doi:10.1175/JAS3615.1, 2005.

Xiao, Q., Kuo, Y.-H., Sun, J., Chaulee, W., and Barker, D. M.: An Approach of RADAR Reflectivity Data Assimilation and Its Assessment with the Inland QPF of Typhoon Rusa (2002) at Landfall, J. Appl. Meteor. Climatol., 46, 14–22, 2007.

Xiao, Q., Kuo, Y.-H., Sun, J., and Lee, W. C.: Assimilation of Doppler RADAR Observations with a Regional 3DVAR System: Impact of Doppler Velocities on Forecasts of a Heavy Rainfall Case, J. Appl. Meteor., 44, 768–788, 2005.

Xu, Q., Wei, L., Gu, W., Gong, J., and Zhao, Q.: A 3.5-dimensional variational method for Doppler radar data assimilation and its application to phased array radar observations, Adv. Meteorol., vol. 2010, Article ID 797265, https://doi.org/10.1155/2010/797265, 2010.

1033 Xue, M., Wang, D., Gao, J., Brewster, K., and Droegemeier, K. K: The Advanced Regional Prediction
1034 System (ARPS), storm scale numerical weather prediction and data assimilation, Meteor. Atmos.
1035 Phys., 82, 139–170, 2003.

1036 Zhao, Q., Cook, J., Xu, Q., and Harasti, P. R.: Using radar wind observations to improve mesoscale
1037 numerical weather prediction, Weather Forecast, 21, 502–522, 2006.

1038

1039 **TABLES**

1040 Table 1: List of physical parameterisations used for RAMS@ISAC in this paper.

Physical parameterization	Selected scheme
Parametrized cumulus convection	Modified Kuo scheme to account for updraft and downdraft (Molinari and Corsetti, 1985). The scheme is applied to R10 only.
Explicit precipitation parameterization	Bulk microphysics with six hydrometeors (cloud, rain, graupel, snow, ice, water vapour). Described in Hong and Lim (2006).
Exchange between the surface, the biosphere and atmosphere.	LEAF3 (Walko et al., 2000). LEAF includes prognostic equations for soil temperature and moisture for multiple layers, vegetation temperature and surface water, and temperature and water vapour mixing ratio of canopy air.
Sub-grid mixing	The turbulent mixing in the horizontal directions is parameterised following Smagorinsky (1963), vertical diffusion is parameterised according to the Mellor and Yamada (1982) scheme, which employs a prognostic turbulent kinetic energy.
Radiation scheme	Chen-Cotton (Chen and Cotton, 1983). The scheme accounts for condensate in the atmosphere.

1041

1042 Table 2: Basic parameters of the RAMS@ISAC grids (R10, R4 and R1, corresponding, respectively, to the domains D1,
1043 D2 and D3). NNXP is the number of grid points in the WE direction, NNYP is the number of grid-points in the NS
1044 direction, NNZP is the number of vertical levels, DX is the size of the grid spacing in the WE direction, DY is the grid
1045 spacing in the SN direction. Lx, Ly, and Lz are the domain extensions in the NS, WE, and vertical directions. CENTLON
1046 and CENTLAT are the coordinates of the grid centres.

1047

	R10, D1	**R4, D2**	**R1, D3**
NNXP	301	401	203
NNYP	301	401	203
NNZP	36	36	36
Lx	3000 km	1600 km	~270 km

Ly	3000 km	1600 km	~270 km
Lz	~22400 m	~22400 m	~22400 m
DX	10 km	4 km	4/3 km
DY	10 km	4 km	4/3 km
CENTLAT (°)	43.0 N	43.0 N	43.7 N
CENTLON (°)	12.5 E	12.5 E	11.0 E

Table 3: Types of simulations performed.

Experiment	Description	Data assimilated	Model variable impacted
CTRL	Control run	None	None
RAD	RADAR data assimilation	Reflectivity factor CAPPI (RAMS-3DVar)	Water vapour mixing ratio
LIGHT	Lightning data assimilation (A=0.85; B=0.16 in Eqn. (1))	Lightning density (nudging)	Water vapour mixing ratio
RADLI	RADAR + lightning data assimilation (A=0.86; B=0.15 in Eqn (1))	Reflectivity factor CAPPI (RAMS-3DVar) + Lightning density (nudging)	Water vapour mixing ratio

1068 Table 4: ETS and POD scores for three different neighbourhood radii. Scores are computed over
1069 the domain D2.

Threshold (mm/3 h)	ETS nearest neighboorhood (CTRL, RAD, LIGHT, RADLI)	POD nearest neighbourhood (CTRL, RAD, LIGHT, RADLI)	ETS 25 km (CTRL, RAD, LIGHT, RADLI)	POD 25 km (CTRL, RAD, LIGHT, RADLI)	ETS 50 km (CTRL, RAD, LIGHT, RADLI)	POD 50 km (CTRL, RAD, LIGHT, RADLI)
1	(0.42,0.36,0.44, 0.33)	(0.57,0.87,0.60, 0.81)	(0.68,0.73,0.68, 0.73)	(0.77,0.93,0.75, 0.89)	(0.79,0.89,0.82, 0.87)	(0.84,0.92,0.84, 0.90)
6	(0.06,0.10,0.14, 0.13)	(0.0,0.5,0.20,0. 72)	(0.11,0.44,0.72, 0.41)	(0.11,0.86,0.72, 0.83)	(0.19,0.86,0.86, 0.92)	(0.19,0.86,0.86, 0.92)
10	(0.,0.05,0.,0.15)	(0.,0.26,0.,0.79)	(0.,0.66,0.58,0. 74)	(0.0,0.84,0.58,0 .89)	(0.,0.95,0.74,0. 90)	(0.,0.95,0.74,0. 90)
20	(0.,0.,0.,0.41)	(0.,0.,0.,0.8)	(0.0,0.41,0.33,0 .87)	(0.,0.47,0.3,0.9)	(0.,0.73,0.80,1. 0)	(0.,0.73,0.80,1. 0)
30	(0.,0.,0.,0.31)	(0.,0.,0.,0.5)	(0.,0.,0.,0.90)	(0.,0.,0.,0.9)	(0.,0.,0.,1.0)	(0.,0.,0.,1.0)
40	(0.,0.,0.,0.)	(0.,0.,0.,0.)	(0.,0.,0.,0.33)	(0.,0.,0.,0.33)	(0.,0.,0.,0.50)	(0.,0.,0.,0.50)

1070

1071

1072 Table 5: ETS and POD scores for three different neighbourhood radii. Scores are computed over
1073 the domain D3.

Threshold (mm/3 h)	ETS nearest neighboorhood (CTRL, RAD, LIGHT, RADLI)	POD nearest neighbourhood (CTRL, RAD, LIGHT, RADLI)	ETS 25 km (CTRL, RAD, LIGHT, RADLI)	POD 25 km (CTRL, RAD, LIGHT, RADLI)	ETS 50 km (CTRL, RAD, LIGHT, RADLI)	POD 50 km (CTRL, RAD, LIGHT, RADLI)
1	(0.43,0.64,0.70, 0.56)	(0.67,0.86,0.98, 0.99)	(0.68,0.80,0.82, 0.71)	(0.83,0.92,0.98, 0.99)	(0.68,0.80,0.82, 0.71)	(0.83,0.92,0.98, 0.99)
6	(0.1,0.31,0.60,0 .49)	(0.24,0.58,0.89, 0.95)	(0.49,0.70,0.91, 0.96)	(0.55,0.76,0.96, 0.97)	(0.49,0.70,0.91, 0.96)	(0.55,0.76,0.96, 0.97)
10	(0.11,0.33,0.56, 0.54)	(0.19,0.56,0.75, 0.80)	(0.48,0.76,0.91, 0.97)	(0.52,0.79,0.92, 0.97)	(0.48,0.76,0.91, 0.97)	(0.52,0.79,0.92, 0.97)
20	(0.02,0.30,0.52, 0.59)	(0.03,0.39,0.74, 0.81)	(0.18,0.73,0.97, 0.93)	(0.19,0.74,0.97, 0.97)	(0.18,0.73,0.96, 0.93)	(0.19,0.74,0.97, 0.97)
30	(0.,0.27,0.51,0. 47)	(0.,0.29,0.76,0. 76)	(0.,0.64,0.94,1.)	(0.,0.65,1.,1.)	(0.,0.64,0.94,1.)	(0.,0.65,1.,1.)
40	(0.,0.44,0.27,0. 27)	(0.,0.44,0.56,0. 67)	(0.,0.89,1.,1.)	(0.,0.89,1.,1.)	(0.,0.89,1.,1.)	(0.,0.89,1.,1.)
50	(0.,0.33,0.66,0. 50)	(0.,0.33,0.67,0. 67)	(0.,0.67,1.,1.)	(0.,0.67,1.,1.)	(0.,0.66,1.,1.)	(0.,0.67,1.,1.)

1074

1075

1076 Table 6 ETS and POD scores for three different neighbourhood radii. Scores are computed over the

1077 domain D2.

Threshold (mm/3 h)	ETS nearest neighboorhood (CTRL, RAD, LIGHT, RADLI)	POD nearest neighbourhood (CTRL, RAD, LIGHT, RADLI)	ETS 25 km (CTRL, RAD, LIGHT, RADLI)	POD 25 km (CTRL, RAD, LIGHT, RADLI)	ETS 50 km (CTRL, RAD, LIGHT, RADLI)	POD 50 km (CTRL, RAD, LIGHT, RADLI)
1	(0.41,0.63,0.61, 0.65)	(0.66,0.89,0.89, 0.93)	(0.79,0.83,0.82, 0.83)	(0.89,0.95,0.95, 0.96)	(0.88,0.92,0.93, 0.94)	(0.93,0.97,0.98, 0.98)
6	(0.2,0.4,0.39,0. 47)	(0.43,0.82,0.77, 0.88)	(0.45,0.63,0.71, 0.76)	(0.63,0.90,0.95, 0.96)	(0.72,0.86,0.88, 0.92)	(0.82,0.96,0.97, 0.96)
10	(0.,0.24,0.18,0. 28)	(0.14,0.78,0.55, 0.80)	(0.14,0.47,0.58, 0.62)	(0.24,0.86,0.82, 0.93)	(0.32,0.91,0.96, 0.95)	(0.35,0.95,0.97, 0.97)
20	(-0.03,0.18,0.13, 0.22)	(0.01,0.81,0.30, 0.80)	(0.09,0.46,0.57, 0.61)	(0.11,0.86,0.59, 0.90)	(0.15,0.84,0.91, 0.96)	(0.15,0.90,0.92, 0.97)
30	(-0.02,0.22,0.13, 0.28)	(0.,0.90,0.23,0. 88)	(0.01,0.79,0.46, 0.80)	(0.01,0.93,0.47, 0.94)	(0.02,0.95,0.93, 0.99)	(0.02,0.95,0.93, 0.99)
40	(-0.1,0.24,0.08,0. 36)	(0.,0.83,0.12,0. 89)	(0.01,0.83,0.37, 0.83)	(0.02,0.97,0.38, 0.97)	(0.1,0.97,0.95,0 .98)	(0.02,0.98,0.95, 0.98)
50	(-0.01,0.27,0.,0.4 3)	(0.,0.67,0.,0.92)	(0.,0.90,0.,0.90)	(0.,0.94,0.,0.96)	(0.,0.96,0.,0.96)	(0.,0.96,0.,0.96)

1078

1079

1080

1081

1082

1083

1084

1085

1086

1087
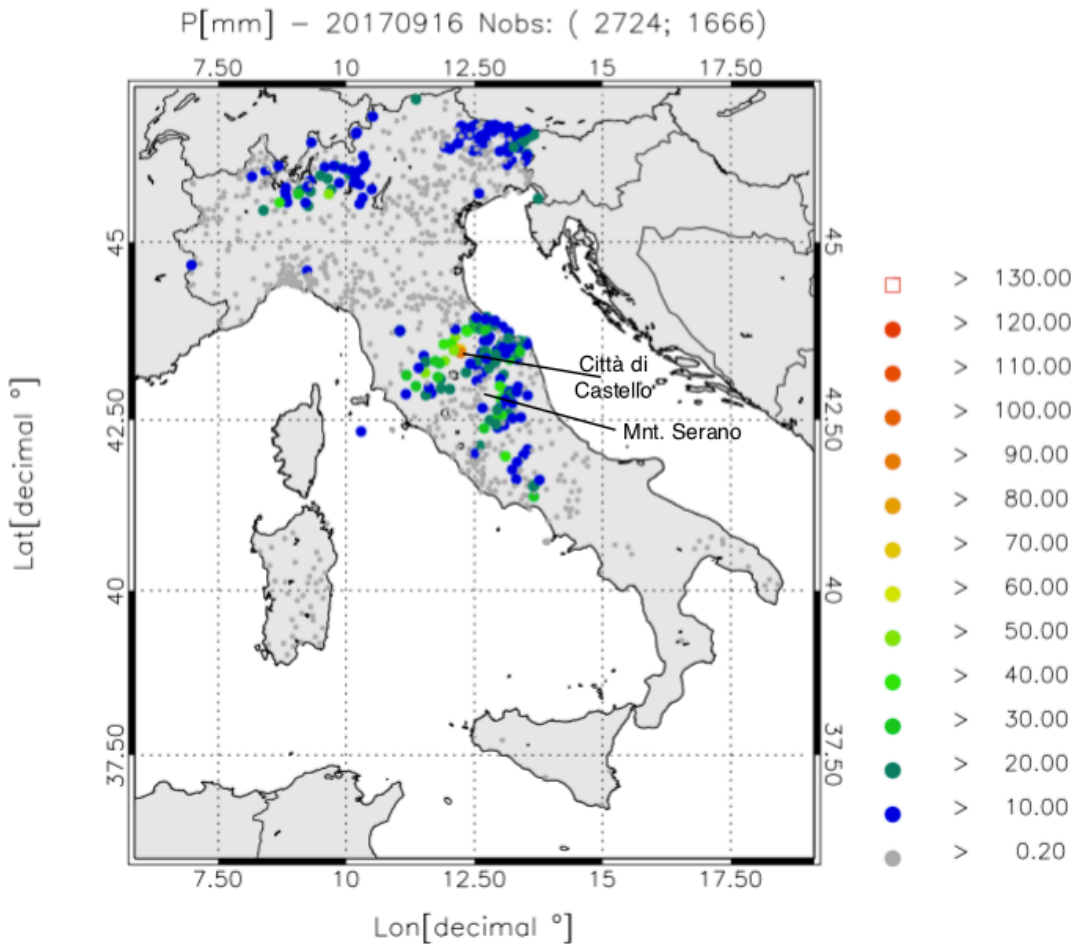
FIGURES

Figure 1: Daily precipitation (P) [mm] over Italy on 16 September 2017. Only raingauges observing at least 0.2 mm/day are shown. The first number in the figure title within brackets represents the available raingauges, while the second number represents raingauges observing at least 0.2 mm/3h. The lowest precipitation class is represented by smaller dots, the largest by a red square. The locations of Città di Castello and Mount Serano are indicated.

1107   a)

HGT[m] - WSP[m/s] - 20170916000000 - z=   500 hPa
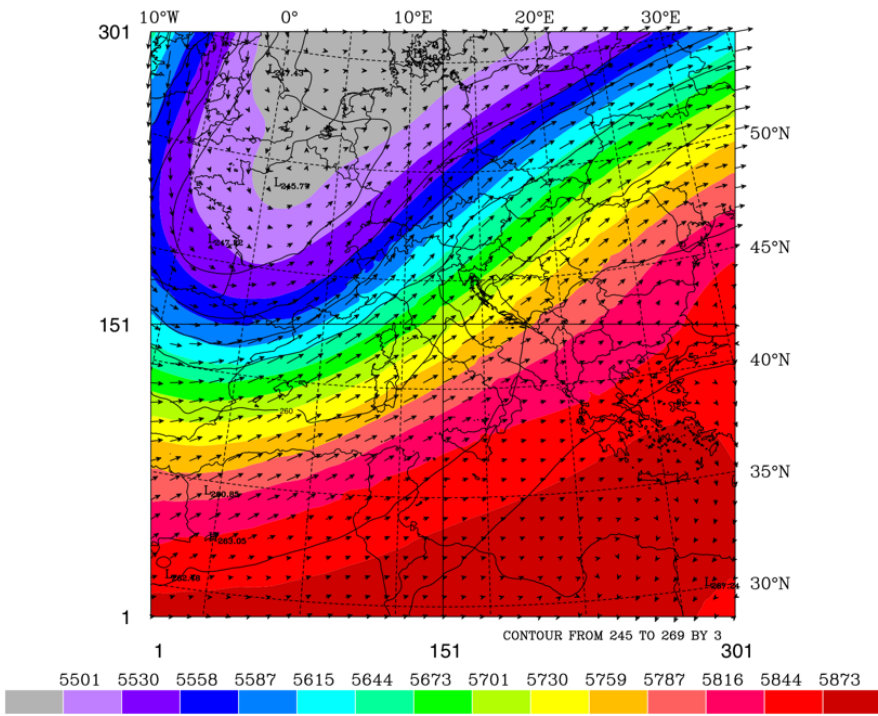
1108

1109   b)
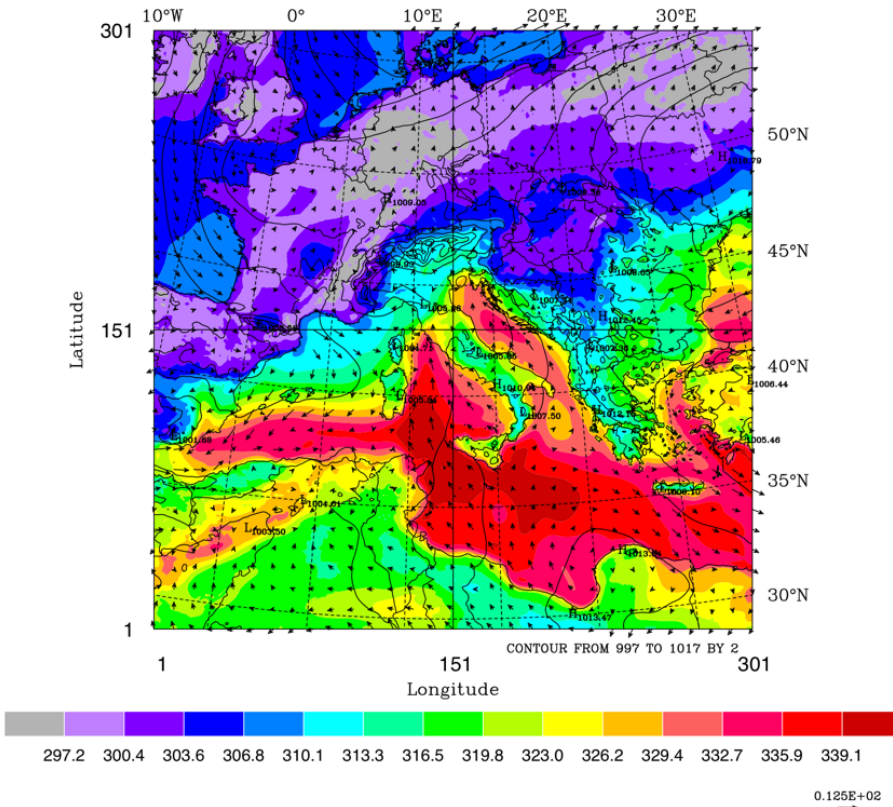
1110

Figure 2: a) Geopotential height (filled contours), temperature (contours) and wind vectors at 500 hPa on 16 September 2017 at 00 UTC. Maximum velocity is 31 m/s; b) equivalent potential temperature (filled contours), sea-level pressure (contours) and wind vectors at 24 m above the surface (first vertical level of RAMS@ISAC, maximum value 13 m/s). A low-pressure patter is forming over northern Italy, with a front in the western Mediterranean.

a)   b)   c)

00UTC 16 sep   *12UTC 16 sep*   *00UTC 17 sep*
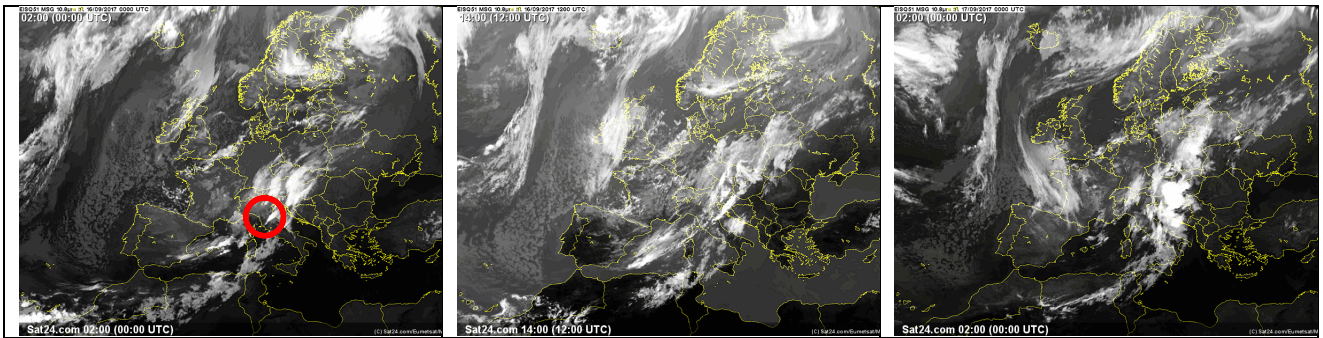
Figure 3: a) Satellite images (METEOSAT second generation) of the infrared channel, 10.8 micron, at 00 UTC and 12 UTC on 16 September, and at 00 UTC on 17 September 2017. A well-defined cloud system is apparent inside the red circle of the image at 00 UTC on 16 September 2017.
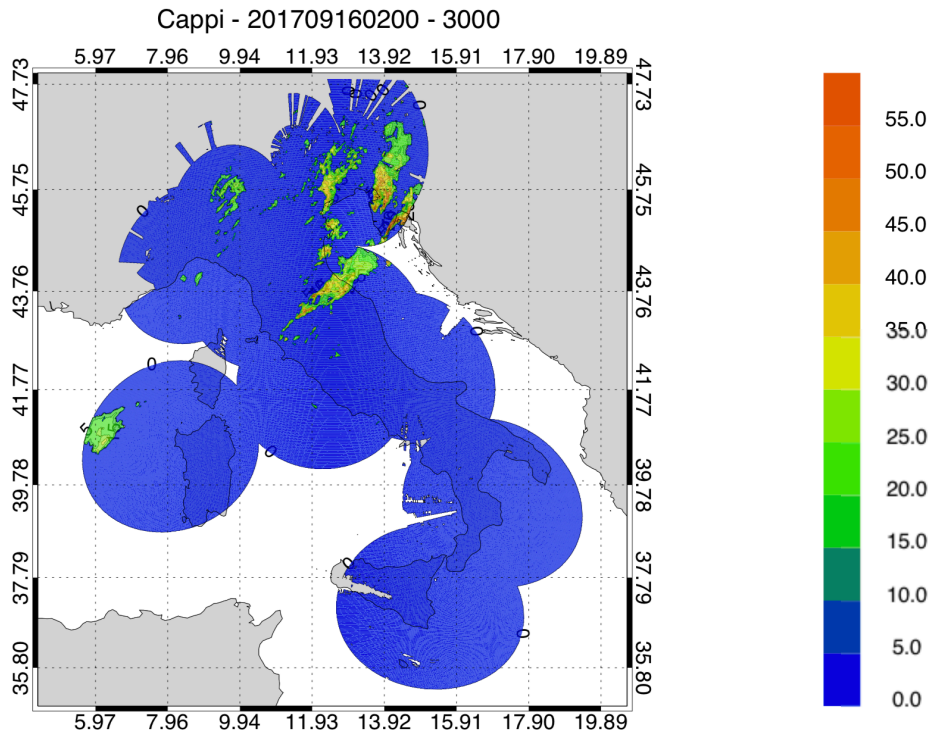
1123

1124   Figure 4: National radar mosaic at 3 km above the sea level observed at 02 UTC on 16 September 2017.

1125
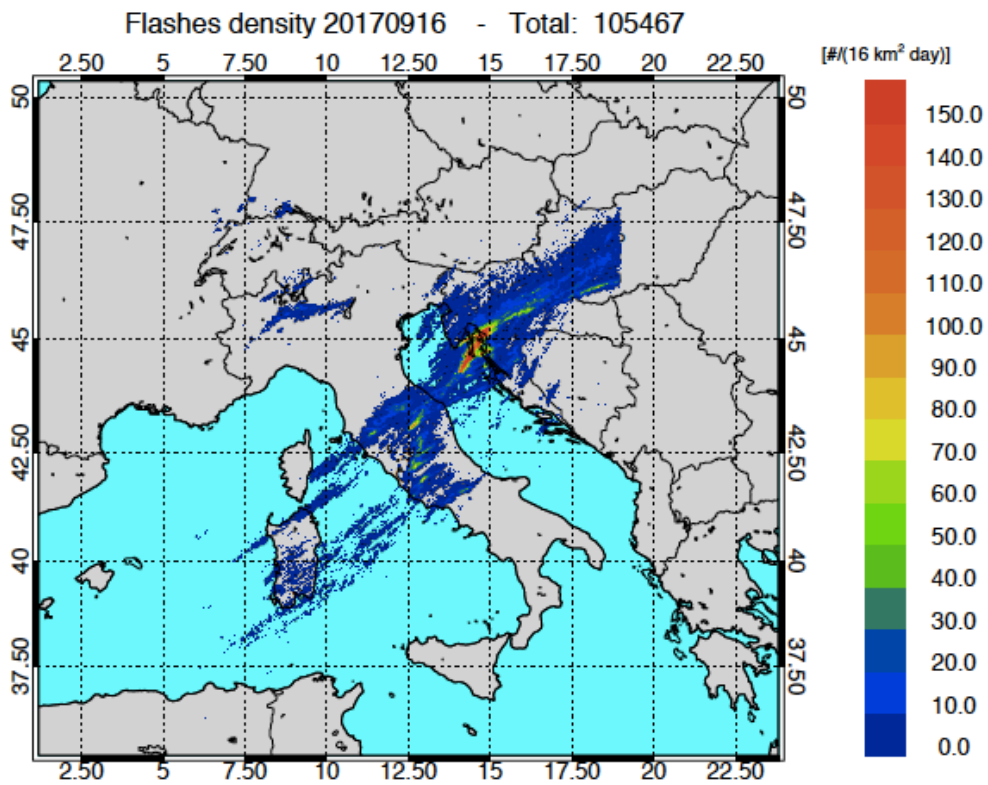
1126

1127   Figure 5: Lightning density (number of lighting per 16 km^2 for the whole day) recorded on 16 September 2017. The
1128   total number of flashes recorded is shown in the title.

1129

1130

1131

1132

1133

1134

1135

1136

1137

1138

1139

1140

1141

1142

1143

1144

1145   a)
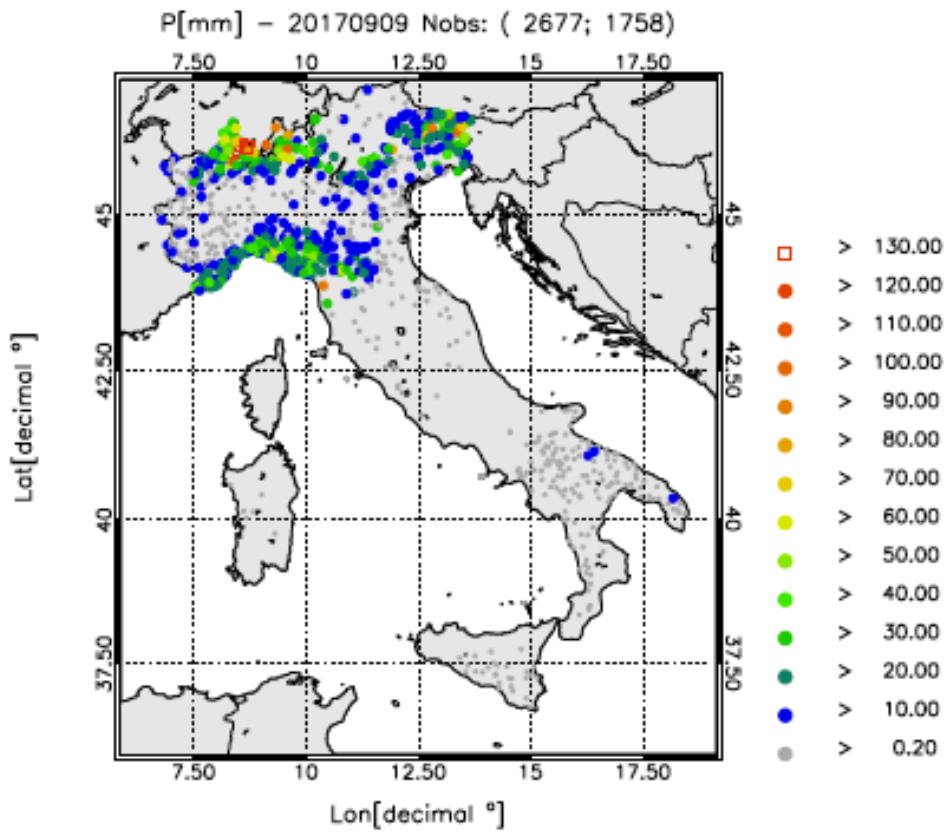
1146

1147   b)
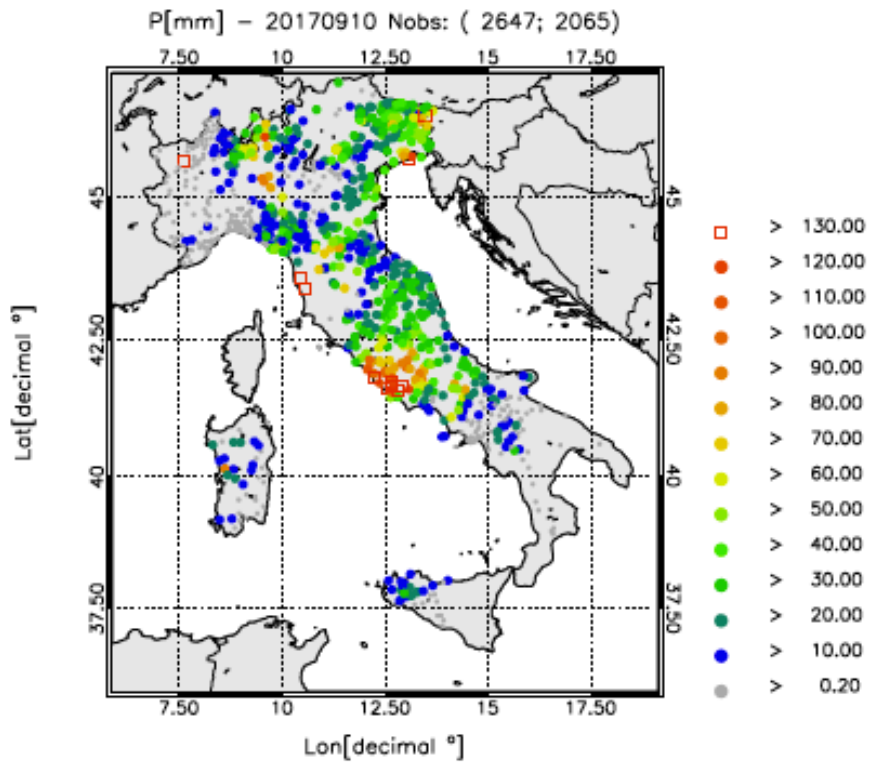
1148

1149   Figure 6: a) As in Figure 1 but for a) 9 September 2017 and b) 10 September 2017.
1150
1151
1152   a)
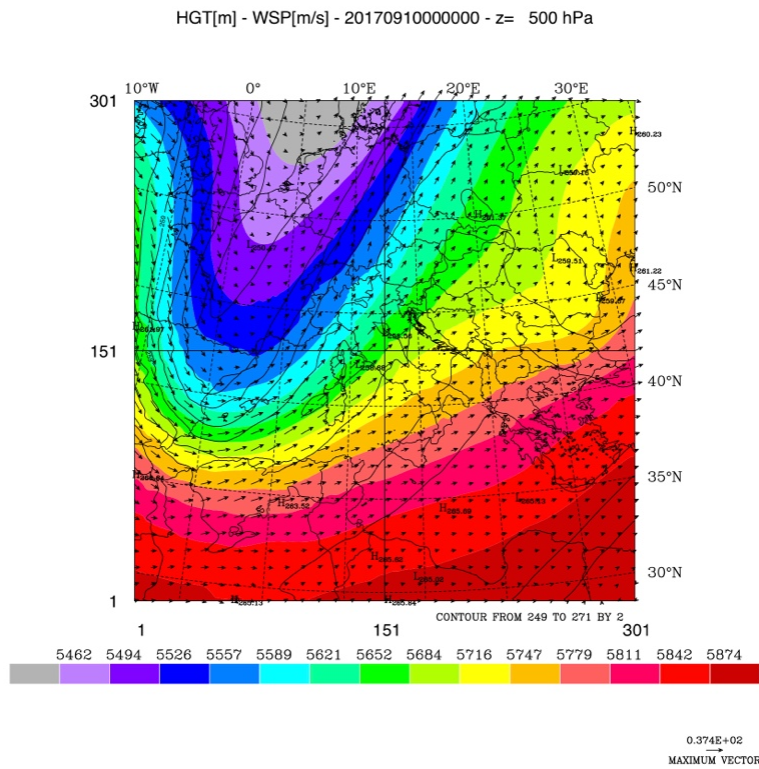
1153

1154   b)
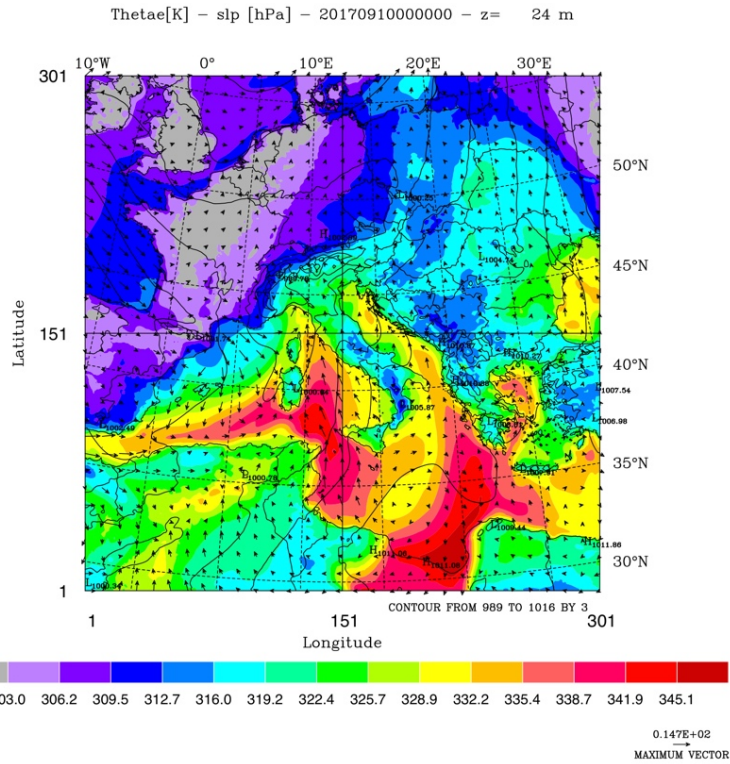
1155

Figure 7: a) Geopotential height (filled contours), temperature (contours) and wind vectors at 500 hPa at 00 UTC on 10
September 2017. Maximum velocity is 37 m/s; b) equivalent potential temperature (filled contours), sea-level
pressure (contours) and wind vectors at 24 m above the surface (first vertical level, maximum value 15 m/s).

1159

1160   a)
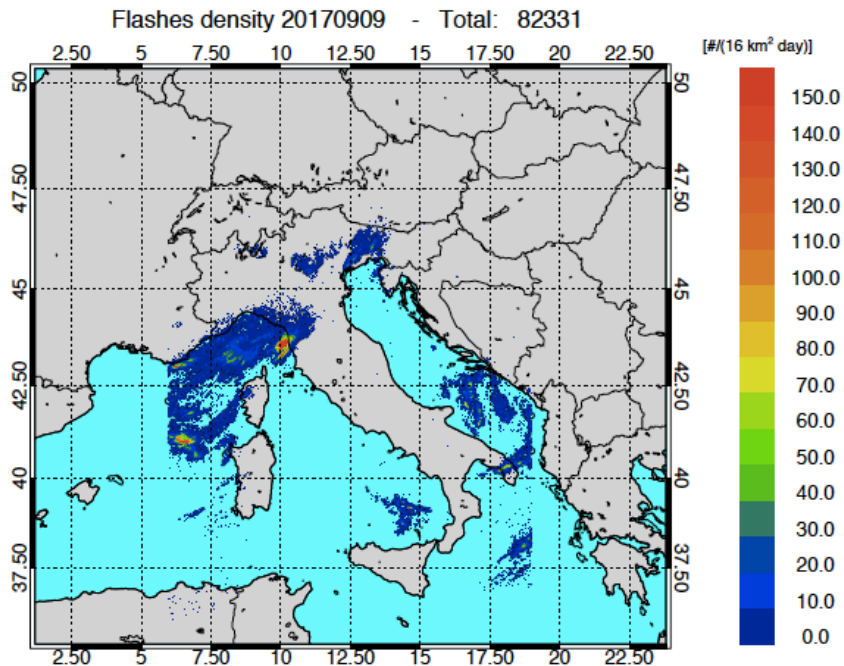
1161

1162

1163

1164   b)
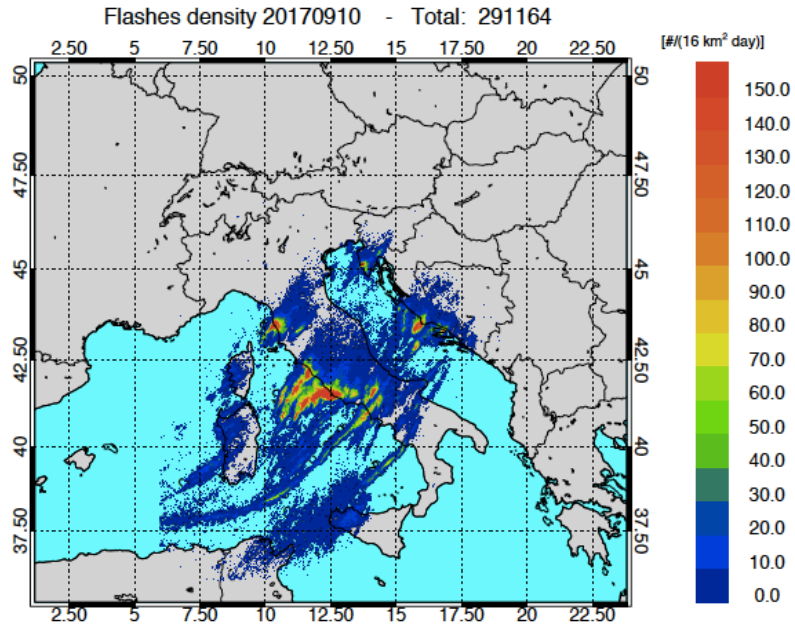
1165

1166 Figure 8: a) Lightning density (lightning number per 16 km² for the whole day) recorded on 09 September 2017; b) as
1167 in a) for 9 September 2017. The number of flashes recorded on each day is shown in the title.

1168

1169

1170

1171

1172   a)   b)   c)
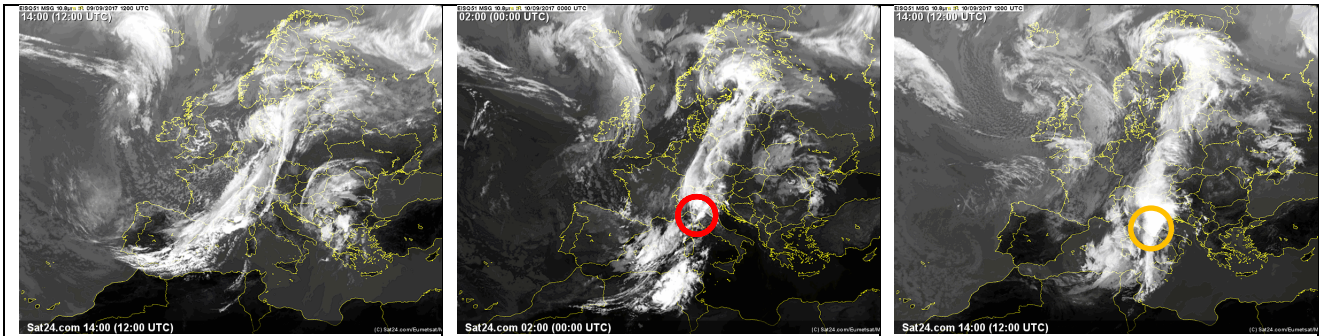
12UTC 09 sep   *00UTC 10 sep*   *12UTC 10 sep*

1173

1174 Figure 9: a) Satellite images (METEOSAT second generation) of the infrared channel, 10.8 micron, at 12 UTC on 9
1175 September 2017, at 00 UTC 00 UTC and 12 UTC on 10 September 2017. The red circle in Figure 9b and the orange
1176 circle in Figure 9c show the Livorno and Lazio area, respectively.

1177

1178

1179

1180

1181

1182

1183   a)
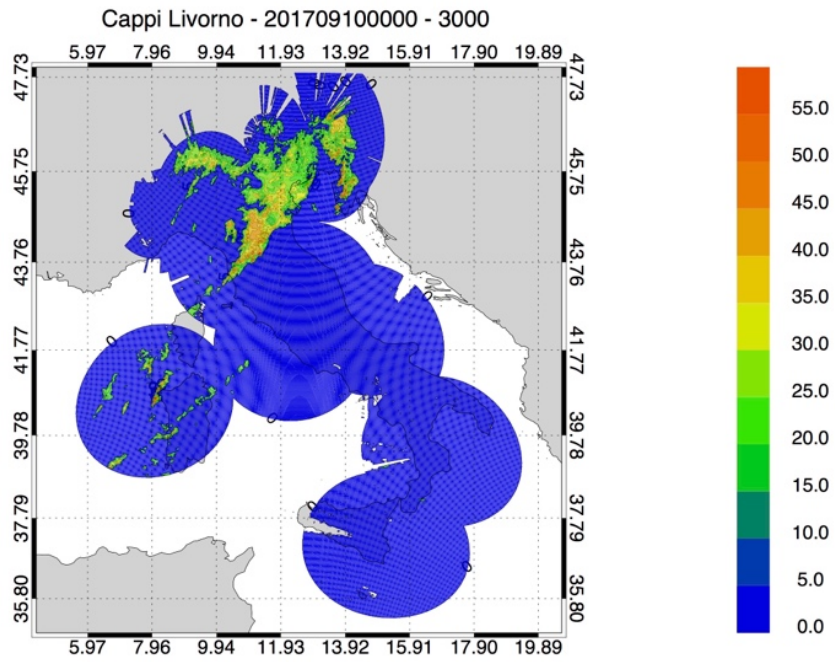
1184

1185   b)
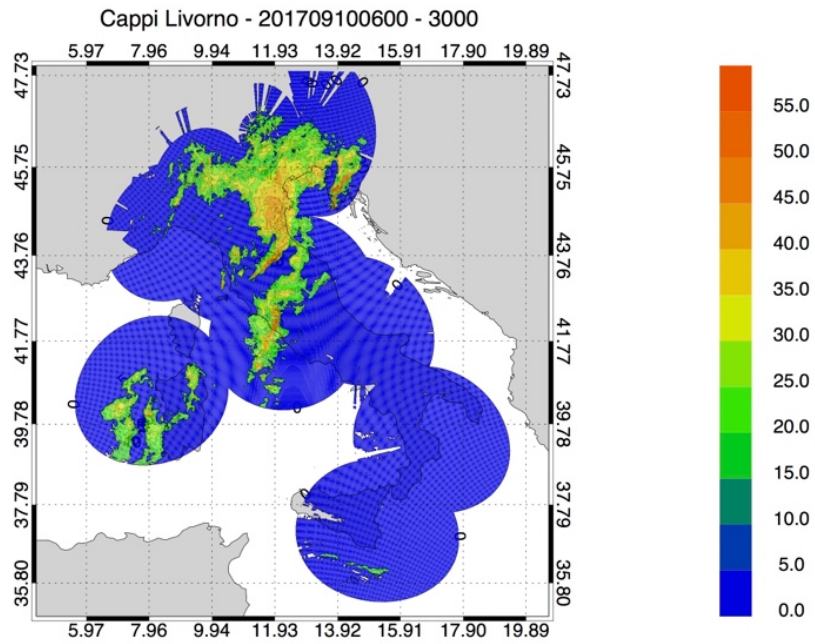
1186

1187   Figure 10: a) National radar mosaic at 3 km above the sea level observed at 00 UTC on 10 September 2017; b) as in a)

1188   at 06 UTC.

1189
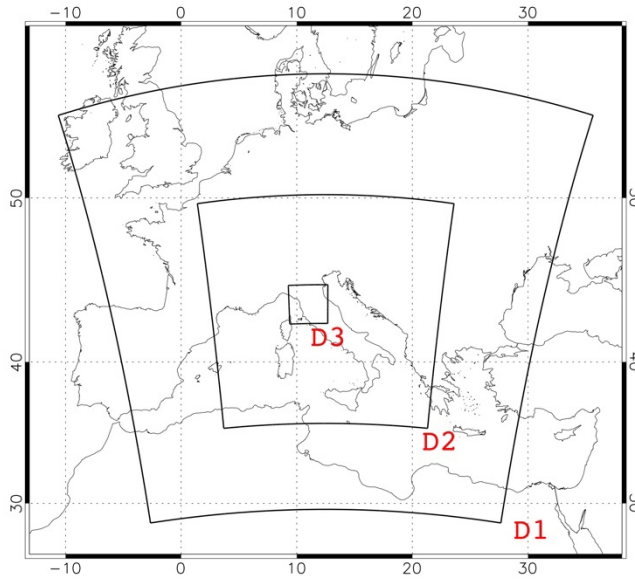
1190

1191   Figure 11: The three domains used in RAMS@ISAC. The model grid over domain D1 has 301 grid points in the NS and

1192   WE directions and has 10 km horizontal resolution, the model grid over domain D2 has 401 grid points in the NS and

1193   WE directions and has 4 km horizontal resolution. The model grid over domain D3 has 203 grid points in the NS and

1194   WE directions and has 4/3 km horizontal resolution. All grids have the same thirty-six vertical levels spanning the 0-

1195   22.4 km vertical layer.
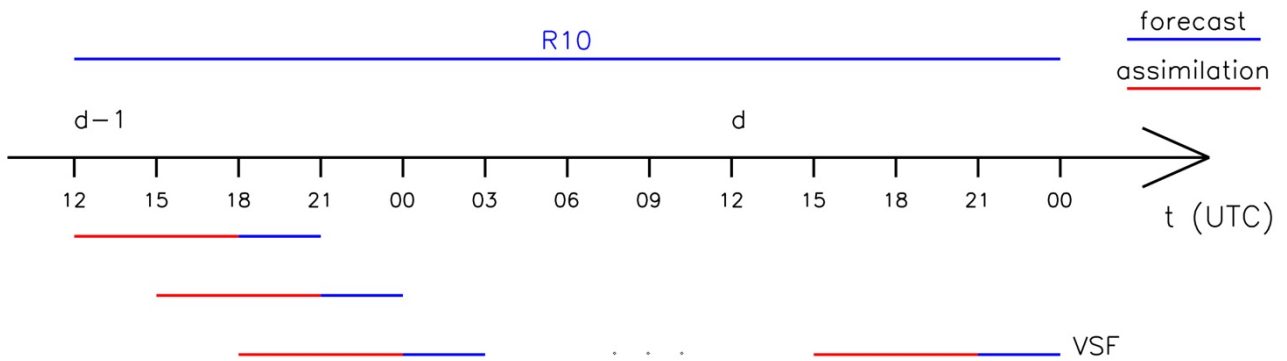
1196

1197   Figure 12: The implementation of RAMS@ISAC very short-term forecast.

1198

Figure 13: The radar network of the Department of Civil Protection. Green radars operate with dual-polarisation, blue radars have single polarisation.

1219   a)
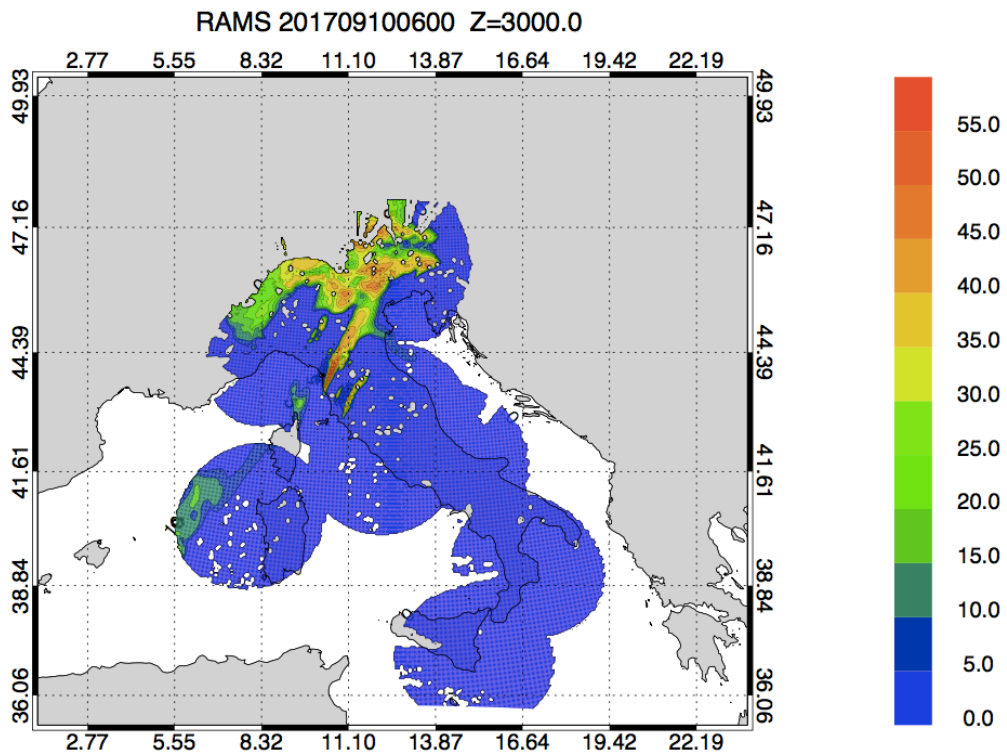
1220

1221   b)
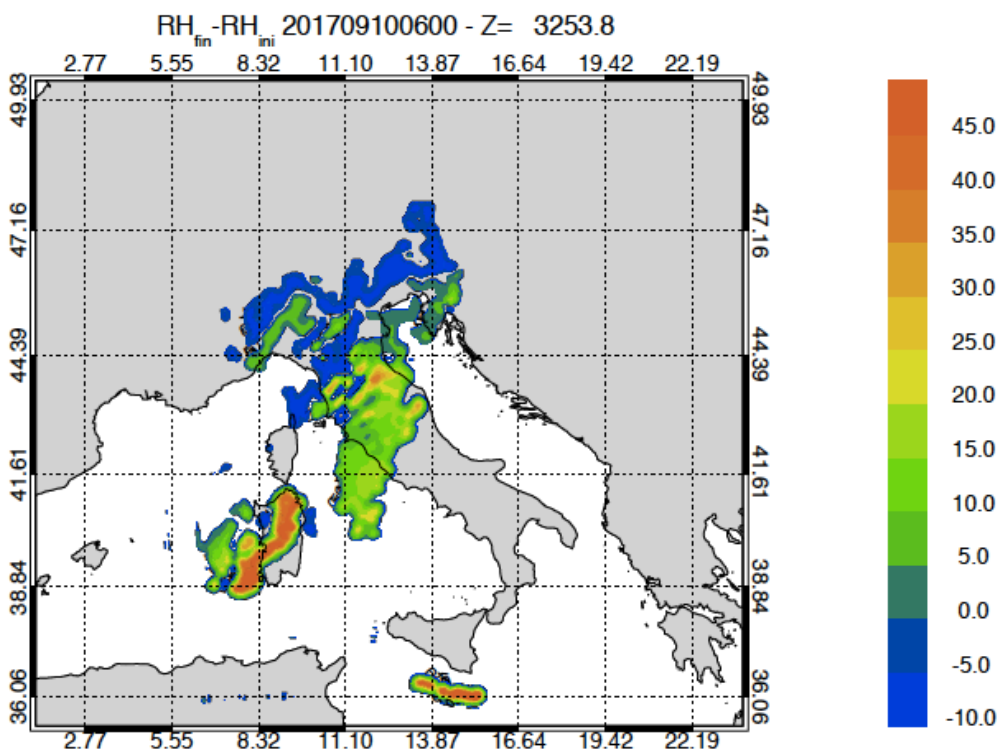
1222

1223   Figure 14: a) RAMS@ISAC reflectivity factor simulated 3 km above sea level at 06 UTC on 10

1224   September 2017; b) relative humidity difference between the analysis and the background at 06

1225   UTC at 3.2 km level in the terrain following vertical coordinate of RAMS@ISAC.

1226

1227   a)
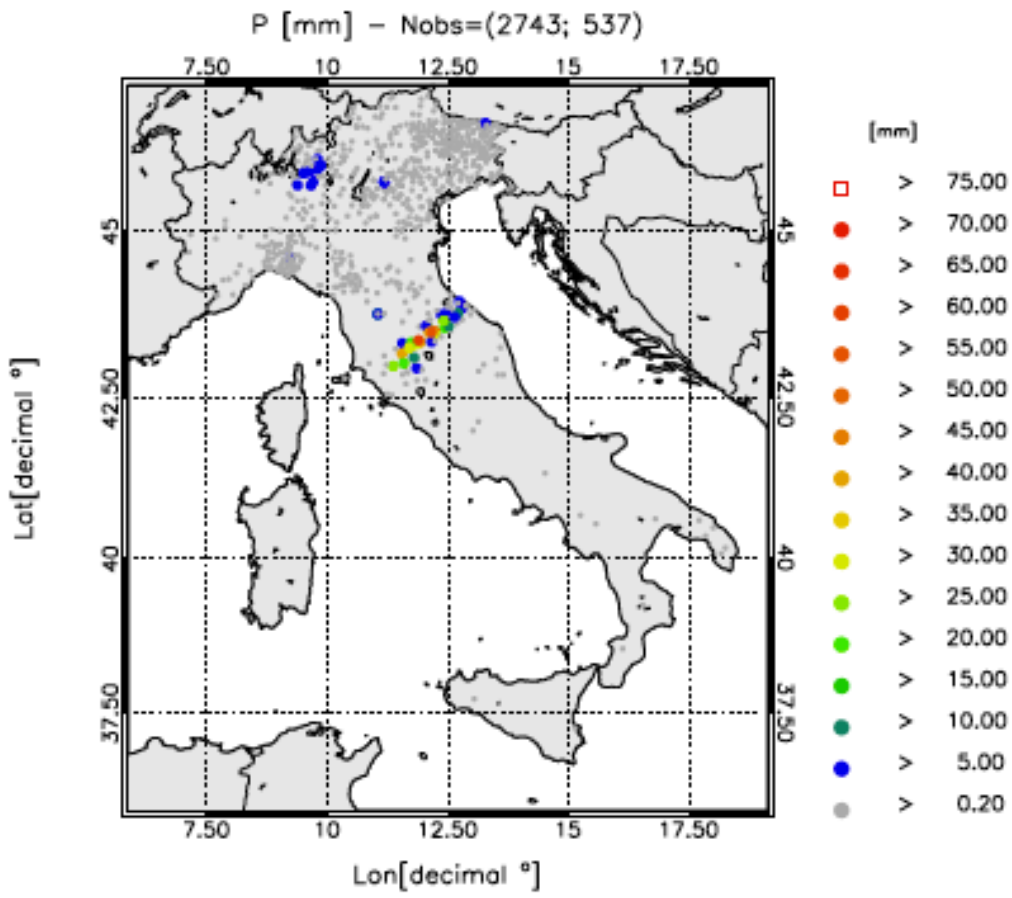
1228

1229

1230   b)
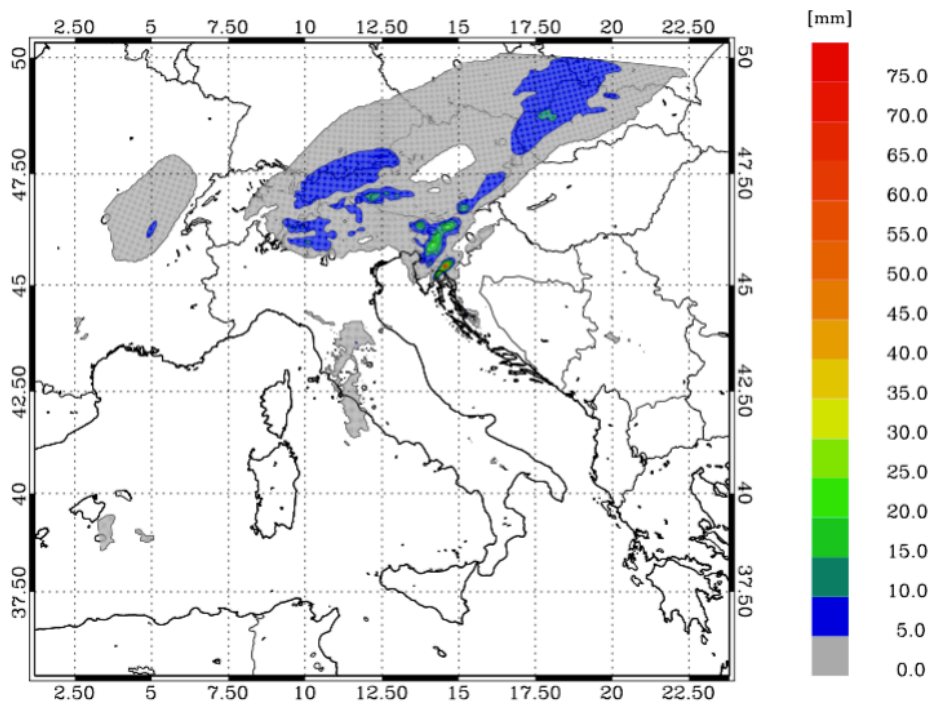
1231

1232

1233   c)

1234
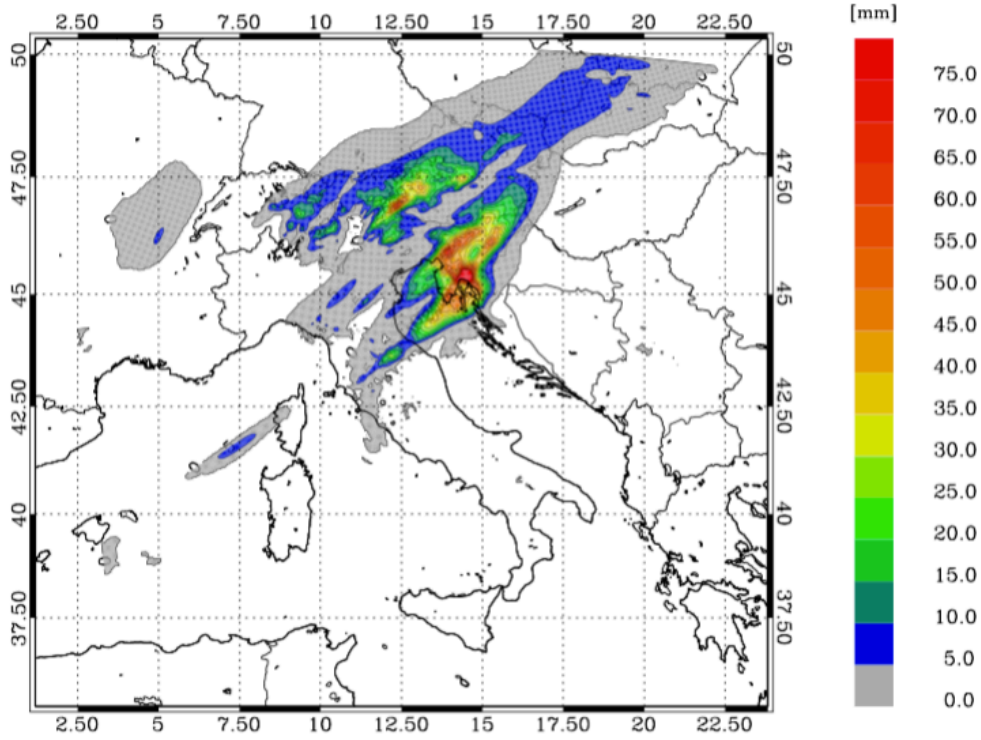
1235

1236

1237

1238   d)

1239
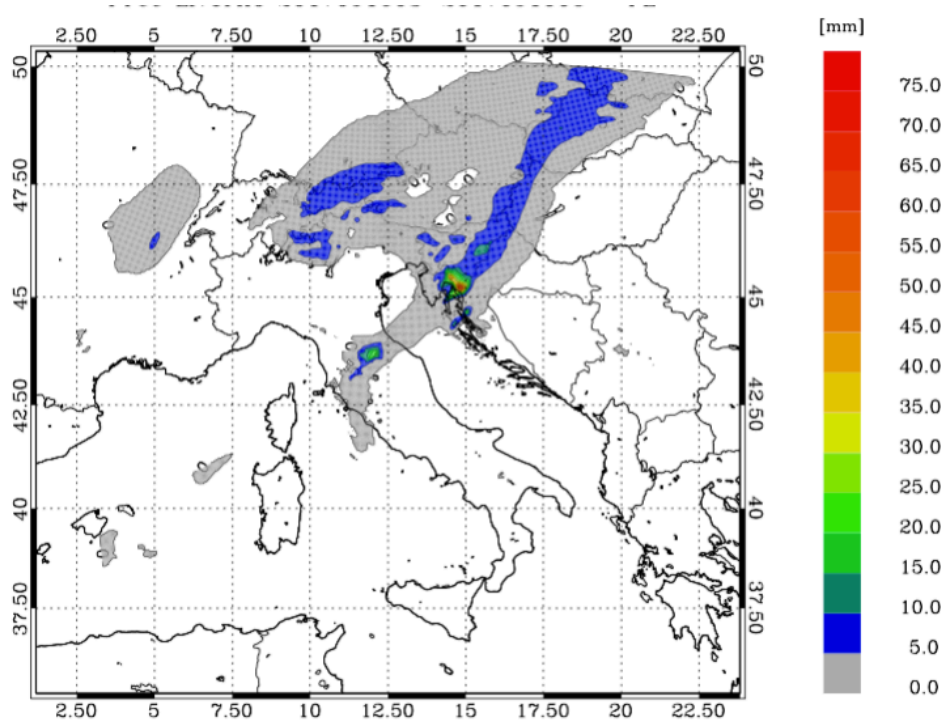
1240

1241

1242   e)
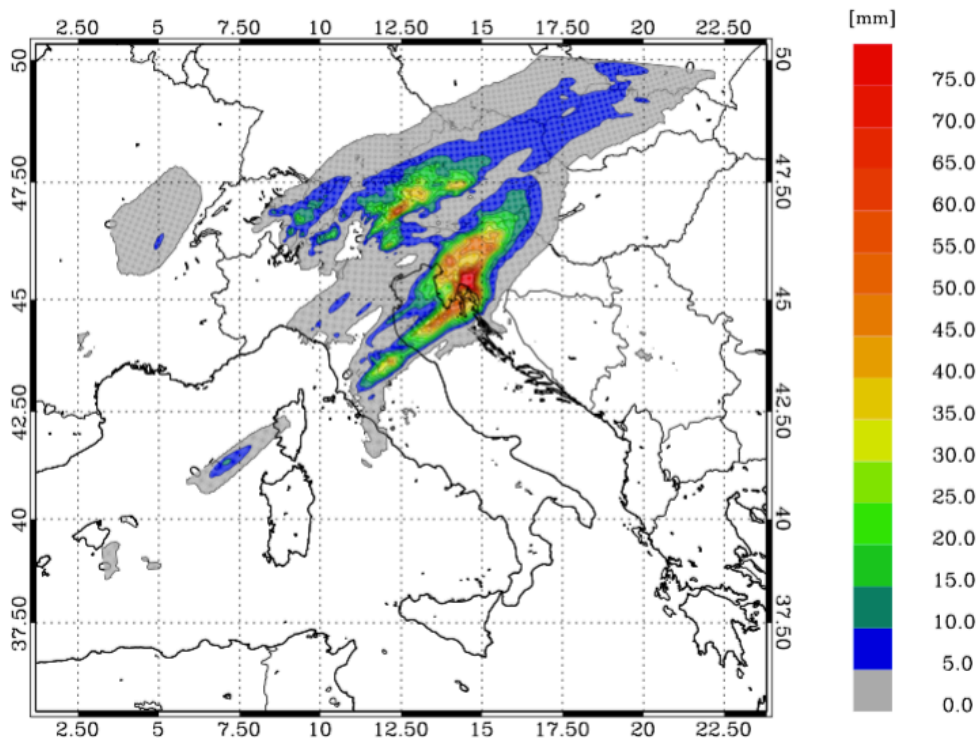
1243

1244   Figure 15: a) rainfall reported by raingauges between 03 and 06 UTC on 16 September 2017. Only raingauges
1245   observing at least 0.2 mm/day are shown. The first number in the title within brackets represents the available
1246   raingauges, while the second number represents those observing at least 0.2 mm/3h; b) rainfall VSF of CTRL for the
1247   same time interval as in a); c) as in b) for RAD forecast; d) as in b) for LIGHT forecast; e) as in b) for RADLI forecast.

1248

1249

1250

1251

1252

1253

1254

1255

1256

1257

1258

1259

1260

1261

1262

1263

1264   a)
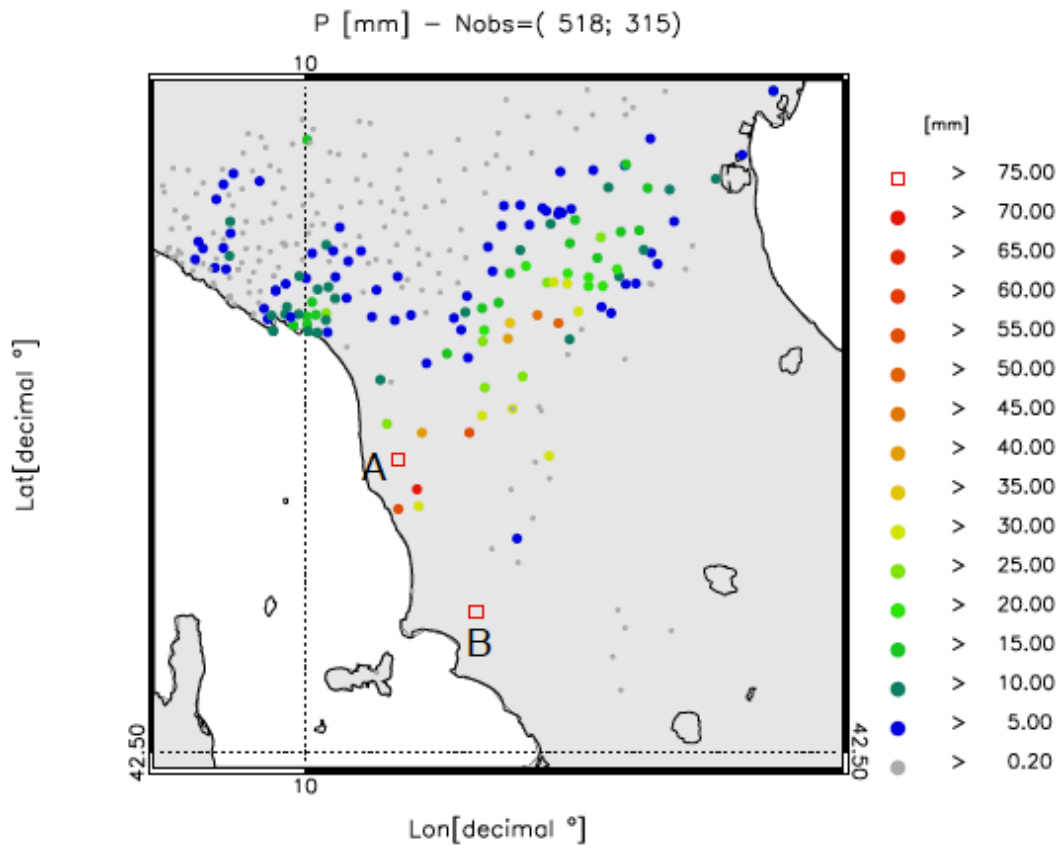
1265

1266   b)
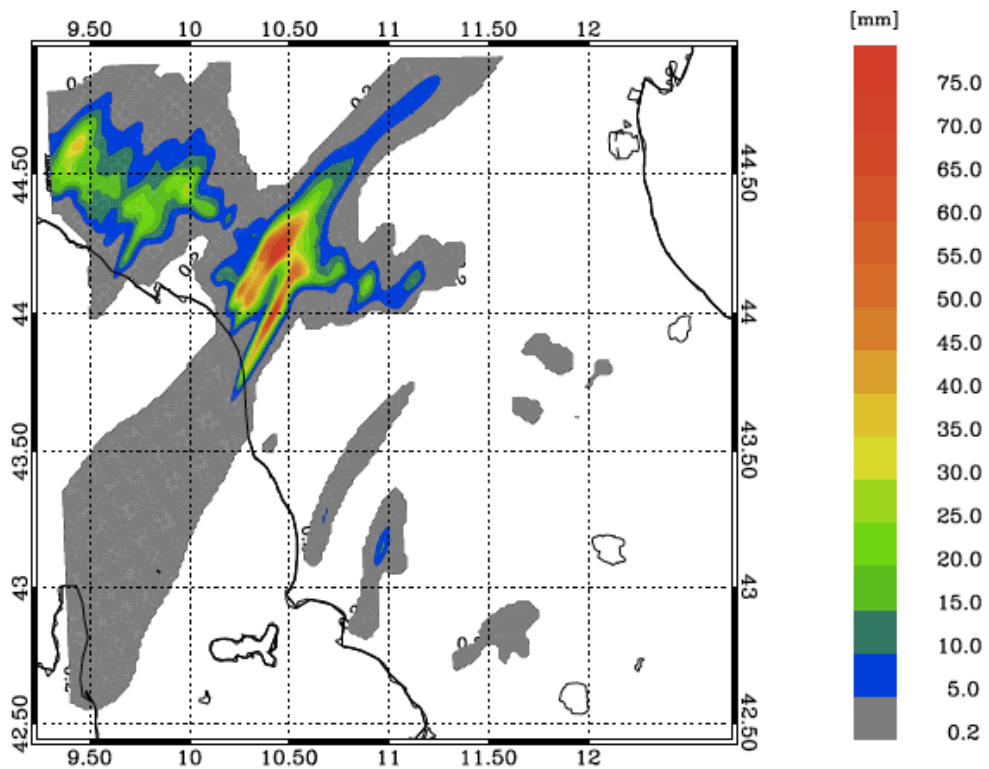
1267

1268

1269

1270 c)
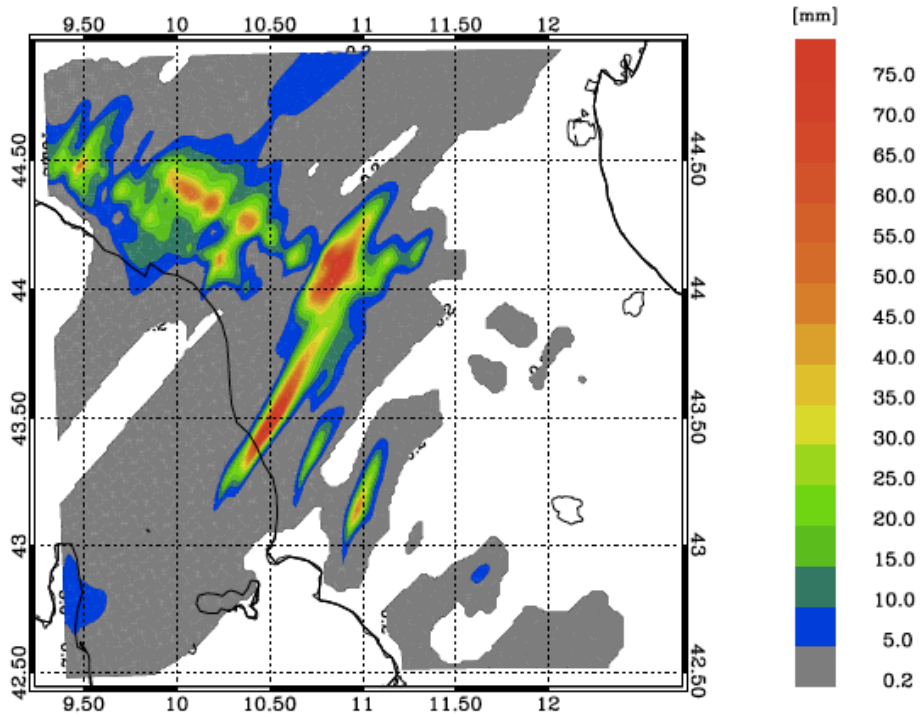
1271

1272

1273 d)
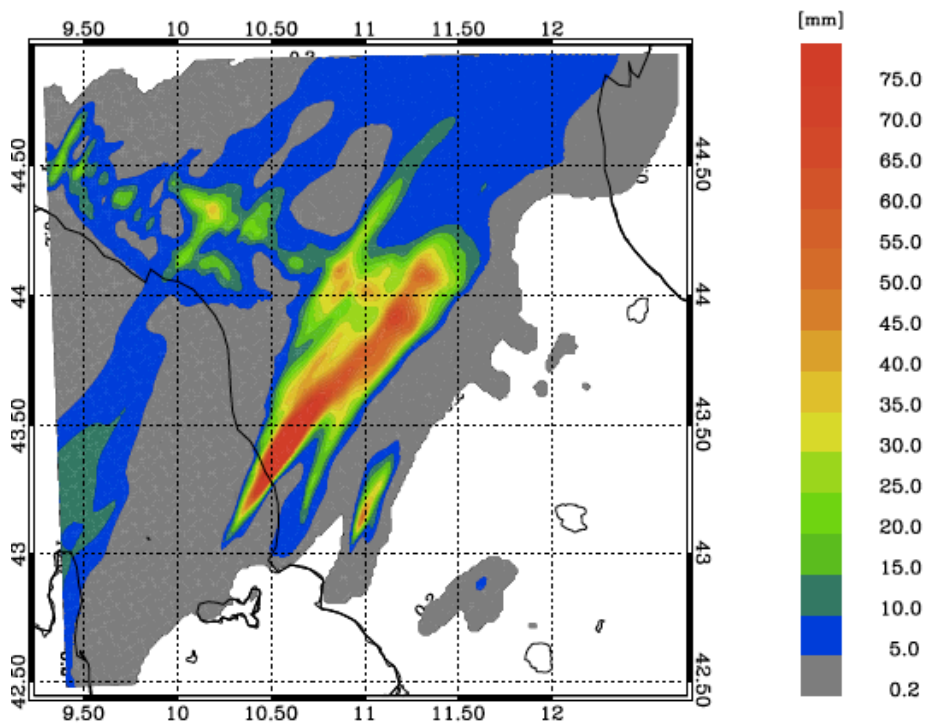
1274

1275

1276

1277

1278

1279

1280   e)

1281
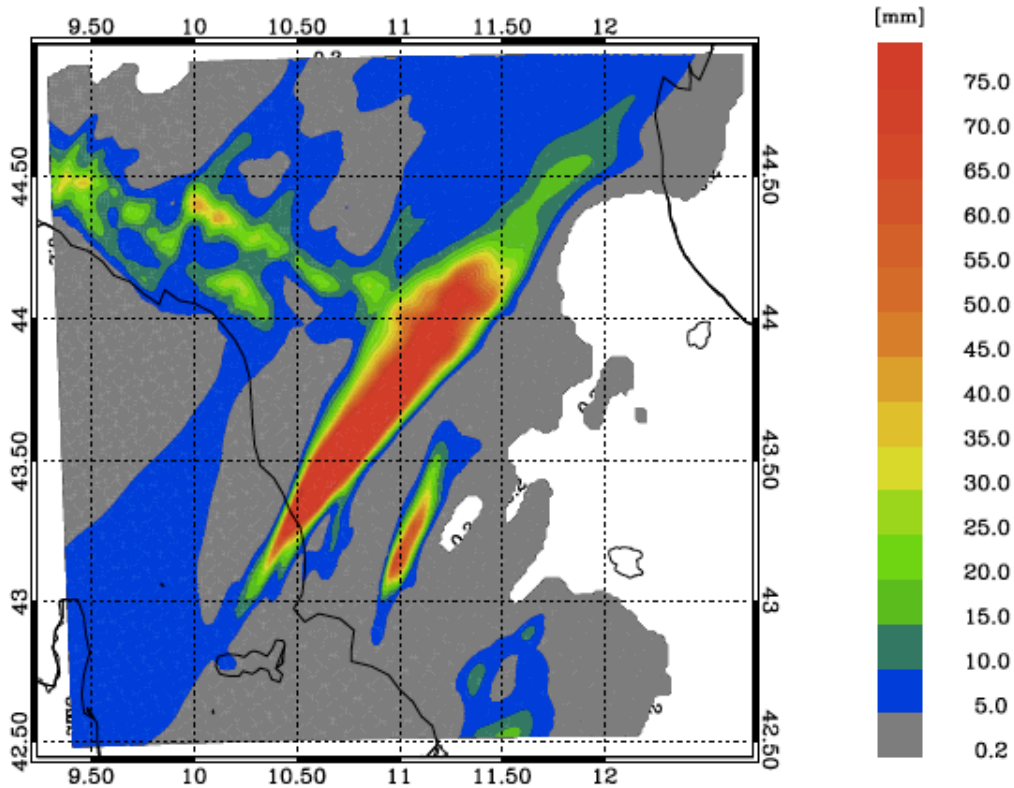
1282

1283

1284   Figure 16: a) rainfall reported by raingauges between 00 and 03 UTC on 10 September 2017. Only stations reporting at
1285   least 0.2 mm/3h are shown. The first number in the title within brackets represents the number of raingauges
1286   available over the domain, while the second number shows those observing at least 0.2 mm/3h; b) rainfall VSF of CTRL
1287   for the same time interval as in a); c) as in b) for RAD forecast; d) as in b) for LIGHT forecast; e) as in b) for RADLI
1288   forecast. Labels A and B help to identify the positions of two rainfall maxima discussed into the text.
1289
1290
1291
1292
1293
1294
1295
1296
1297
1298
1299
1300
1301
1302
1303
1304
1305
1306
1307
1308
1309

1310
1311   a)
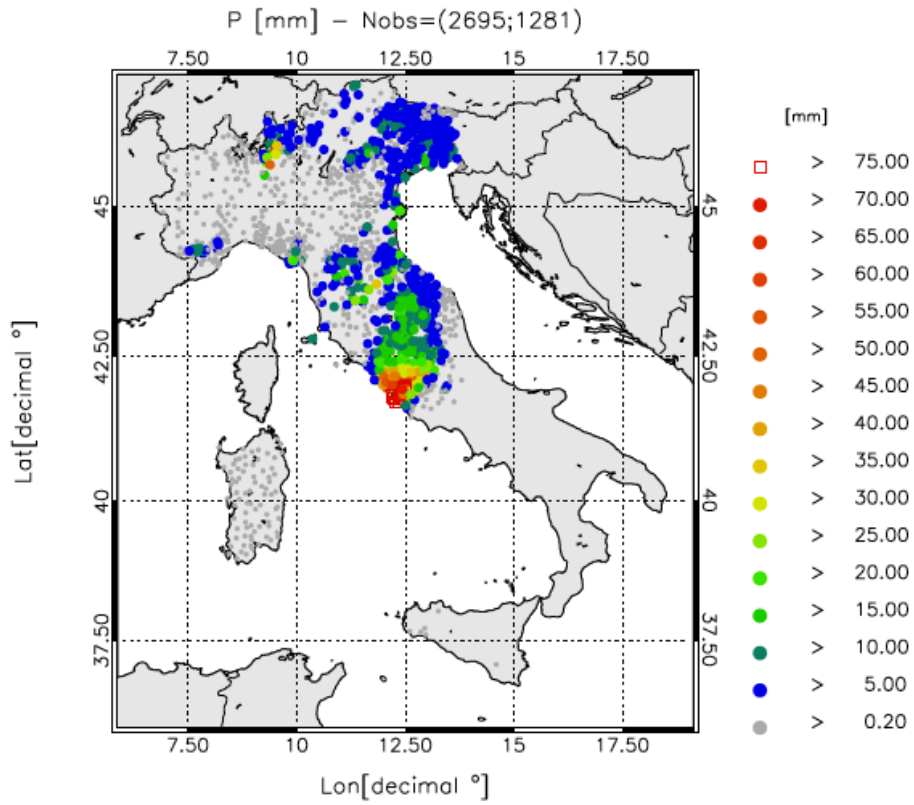
1312
1313   b)
1314
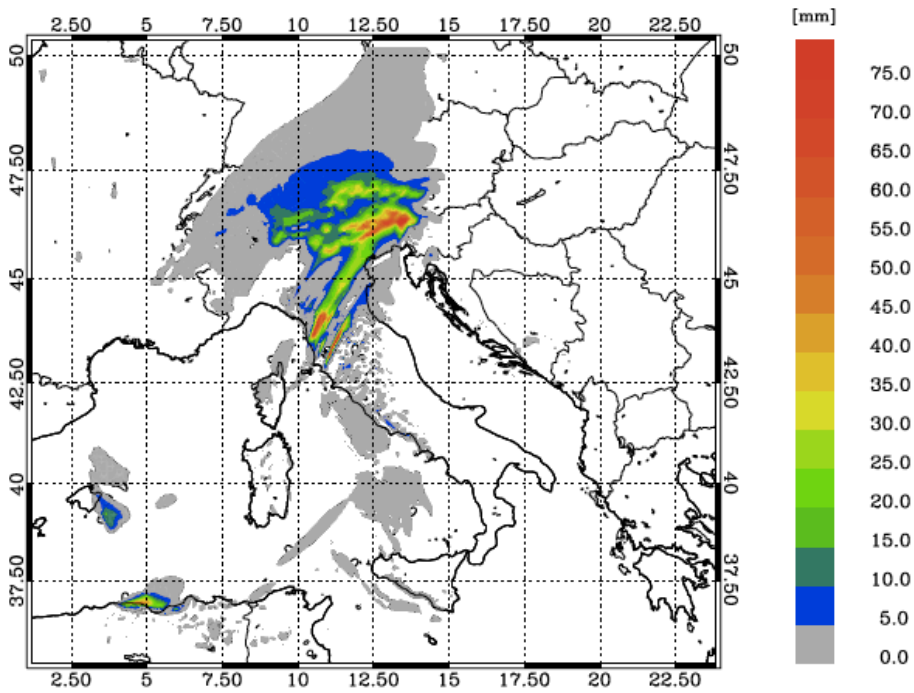
1315
1316
1317

1318

1319   c)
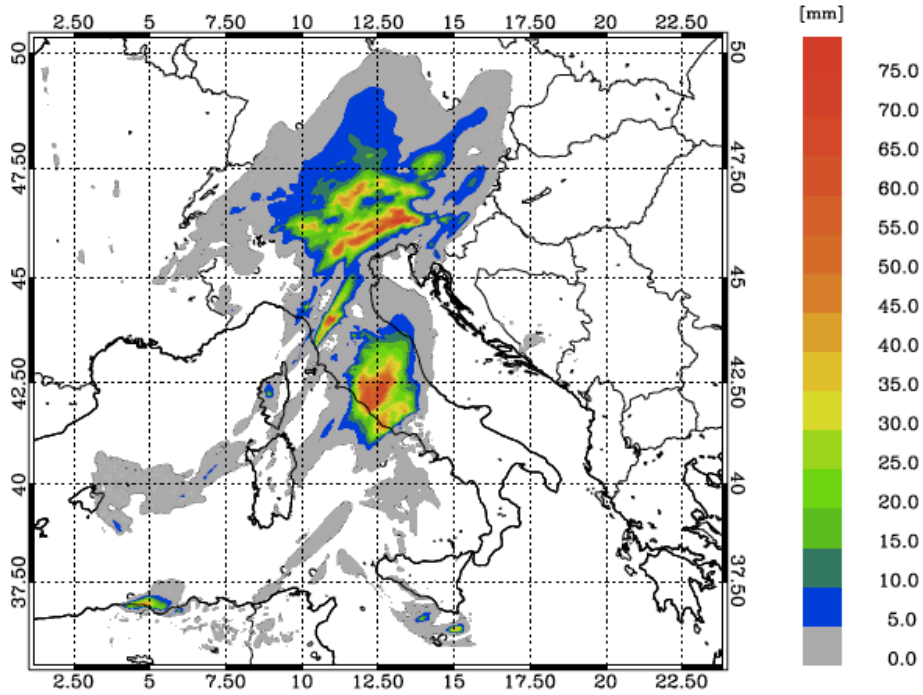
1320
1321

1322   d)
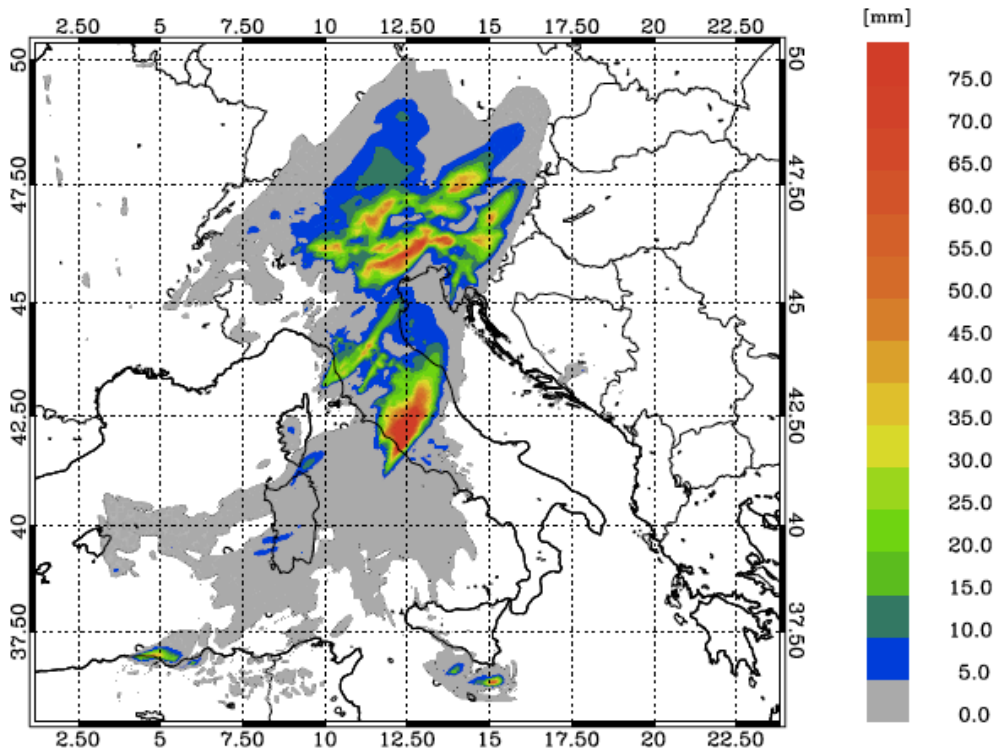
1323
1324
1325
1326

1327

1328   e)
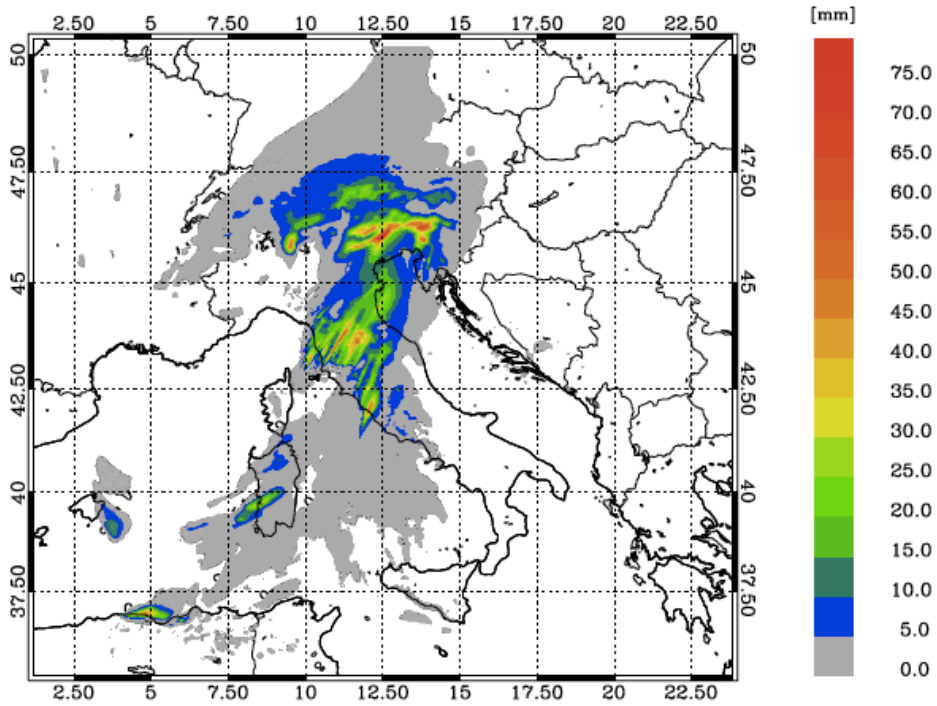
1329

1330   Figure 17: a) rainfall reported by raingauges between 06 - 09 UTC on 10 September 2017. For this time period 2695
1331   raingauges reported valid observations in the domain, however only stations reporting at least 0.2 mm/3h are shown
1332   The first number in the title within brackets represents the number of raingauges available over the domain, while the
1333   second number shows those observing at least 0.2 mm/3h; b) rainfall VSF of CTRL in the same time interval as a); c) as
1334   in b) for RAD forecast; d) as in b) for LIGHT forecast; g) as in b) for RADLI forecast.

1335
1336